Master's Degree Course in Telecommunication Engineering

DEPARTMENT OF INFORMATION ENGINEERING

UNIVERSITY OF PADOVA

Design, simulation and experimental evaluation of indoor localization schemes for 60 GHz millimeter wave systems

Candidate:

Alain OLIVIER

Thesis Supervisor:

Professor Michele ZORZI

Thesis Co-Supervisor:

Professor Paolo CASARI

Graduation Date: October 12th, 2015

Academic Year 2014/2015

UNIVERSITÀ
DEGLI STUDI
DI PADOVA

DEPARTMENT OF
INFORMATION
ENGINEERING
UNIVERSITY OF PADOVA

DESIGN, SIMULATION AND EXPERIMENTAL EVALUATION
OF INDOOR LOCALIZATION SCHEMES
FOR 60 GHZ MILLIMETER WAVE SYSTEMS

by

Alain OLIVIER

Submitted in partial fulfillment of the requirements for the degree

of Master of Science in Telecommunication Engineering

at the

University of Padova

October 2015

Signature of Author_____

Certified by_____

Michele ZORZI, Thesis Supervisor

Dedicated to my parents, Alice, and Elena

ABSTRACT

This thesis targets localization schemes for single-anchor MilliMeter Wave (MMW) systems. After a review of the main propagation properties of MMW signals that may have an impact on localization, we design three algorithms, namely a triangulation-validation procedure, an angle difference-of-arrival approach, and a scheme based on location fingerprinting. With the aid of a ray tracing tool developed for this purpose, the algorithms are evaluated by means of simulations that make it possible to draw initial conclusions about their robustness. The obtained results are then validated via measurements involving commercial pre-standard 60-GHz MMW hardware, showing that by relying only on a single anchor, the algorithms can localize a node with high probability, and in many cases with sub-meter accuracy. After drawing our concluding remarks, we discuss possible extensions of the algorithms.

SOMMARIO

In questa tesi vengono sviluppati algoritmi di localizzazione per sistemi a onde millimetriche basati su un singolo nodo ancora. Dopo aver compreso le principali caratteristiche delle onde millimetriche, vengono delineati tre algoritmi: un primo basato su una procedura di triangolazione-validazione, un secondo basato su differenze dell'angolo di arrivo, e infine un terzo basato sul fingerprinting. Attraverso un ray tracer sviluppato appositamente, gli algoritmi sono poi testati attraverso delle simulazioni al fine di trarre alcune considerazioni riguardanti la precisione e la robustezza ottenibili. Gli algoritmi sono poi testati sperimentalmente attraverso misure su apparecchiature standardizzate a 60 GHz: ne risulta una performance caratterizzata da un'alta probabilità di successo nello stimare la posizione che, in molti casi, raggiunge una precisione inferiore al metro. Infine vengono discussi possibile estensioni e miglioramenti degli algoritmi.

TABLE OF CONTENTS

LIST OF FIGURES

LIST OF TABLES

LIST OF ALGORITHMS

1

INTRODUCTION

Nowadays, emerging MilliMeter Wave (MMW) wireless communication systems represent more than a century of evolution in modern communications. Since the first developed and commercialized wireless telegraph by Guglielmo Marconi in the early 1900s, the wireless industry has expanded from point-to-point technologies, to radio broadcast systems, and finally to wireless networks. As the technology has advanced, wireless communications have become pervasive in our world. We find ourselves fully immersed in wireless networking, as most of us routinely use cellular networks, wireless local area networks, and personal area networks. This has rapidly led to what is known as spectrum crunch or congestion, i.e., the potential lack of sufficient wireless frequency resources needed to support a growing number of consumer devices. Possible solutions to mitigate the spectrum crunch would be to devise communication systems with higher spectrum efficiency, reallocate some frequencies in order to free up capacity, or exploit those frequency bands that actually are not congested. This last point is the motivation behind the recent interest in MMWs, as they are addressed as a possible solution to solve the spectrum congestion problem [2, 3].

The MMW available spectrum, ranging between 30 GHz and 300 GHz, is unparalleled compared to cellular and Wireless Local Area Network (WLAN) microwave systems that operate at frequencies below 10 GHz. For example, the unlicensed frequency band at 60 GHz offers 10× to 100× more spectrum than is available for conventional unlicensed wireless local area networks in the Industrial, Scientific, and Medical (ISM) bands (e.g., at 900 MHz, 2.4 GHz, 5 GHz) or for users of Wireless Fidelity (WiFi) and 4G (or older) cellular systems that operate at carrier frequencies below 6 GHz [2]. Moreover, the availability of a larger bandwidth makes it possible to achieve higher data rates for comparable modulation techniques, i.e., having similar spectrum efficiency, while also providing more resources to be shared among multiple users.

Actually, the MMW spectrum, is occupied by military, radar, and backhaul, but has much lower utilization compared to lower frequencies. Given the large amount of spectrum available, MMW presents a new opportunity for future mobile communications to use channel bandwidths of 1 GHz or more. For example, the spectrum at 28 GHz, 38 GHz, and 70–80 GHz has propagation characteristics that look promising for next-generation cellular systems like 5G [4, 5]. The 60 GHz unlicensed band is seeing active commercial deployment in consumer devices through IEEE 802.11ad [6], a standard also known as WiGig.

Beside communication systems, radio waves have also been addressed as an enabling technology for the development of localization systems. Nowadays, localization systems such as the Global Positioning System (GPS) have become pervasive in our lives in the same way of communication systems. A lot of effort has been put into outdoor localization, whereas indoor localization is a relatively recent field of research, also motivated by the fact that outdoor positioning systems result to be inapplicable due to the low accuracy obtained in indoor environment. Interest on Indoor Positioning Systems (IPSs) have become even more popular in recent years due to the incredible boom of smartphones and tablets in our society, and the upcoming Internet of Things (IoT): some examples are the location detection of products stored in a warehouse, of medical personnel or equipment in a hospital, of firemen in a building on fire, of police dogs trained to find explosives in a building, and of tagged maintenance tools and equipment scattered all over a plant. Clearly, with the advance of communication systems exploiting MMW frequencies, there comes an attempt to devise IPSs that may exploit the future MMW infrastructure. Many solutions have been designed for the ISM frequency bands, exploiting lateration, triangulation and other classic localization techniques [7]. However, since MMW technology has began to emerge recently, the research work is limited and presently there are no schemes devised to exploit the peculiar characteristics of MMW propagation, which are briefly discussed on the remainder of this section. Due to the high path loss (as per Friis transmission equation), and, moreover, the high attenuation due to physical effects, such as rain, steam and oxygen absorption and localized at different intervals of frequency

[5, 8, 9], MMW systems necessitate to employ high-gain directive antennas, thus equipped with steerable mechanisms. At 60 GHz the channel presents an absorption peak due to oxygen absorption: whenever this could be limiting for outdoor communications, it could be positive for indoor applications to due the possibility of limiting the signal inside the building [9]. The small wavelength suggests the possibility of exploiting Multiple-Input Multiple-Output (MIMO) in order to achieve time diversity [10]. Further studies have indicated that mm-wave propagation behaves like quasi-optical, thus the Line of Sight (LoS) component is dominant [11].

1.1 MOTIVATION AND CONTRIBUTION

This thesis was completed mainly as the result of my abroad experience: from March 2015 until the end of August 2015, I have been an internship student at the IMDEA Networks Institute,[1] Madrid, Spain. During my stay, I was directly supervised by Prof. Paolo Casari, and became part of his Ubiquitous Wireless Networking research group. As it has been said, in the recent literature, there does not exist a large bulk of material related to indoor localization that specifically exploits the peculiar characteristics of MMWs. Thus, my work was addressed to devise, analyze and implement a localization scheme suitable for MMW frequencies.

During my first period at the institute I focused on acquiring the necessary knowledge related to the propagation of MMWs. After a further study about localization techniques I decided to devise a localization scheme based on single a Access Point (AP) and the resulting signal reflections off the room boundaries, thus exploiting the quasi-optical behavior of MMWs. Then, I developed a ray tracer useful to simulate the waves propagation inside a room and performed a performance evaluation of the devised algorithm. Aiming to solve different problems led to the development of three different localization schemes, namely, Triangulate-

---

1 IMDEA Networks Institute. Address: Avda. del Mar Mediterraneo 22, 28918 Leganés, Madrid. URL: http://www.networks.imdea.org

Validate (TV), Angle Difference-of-Arrival (ADoA) and Fingerprinting (FP). The three algorithms appeared to be promising and a further characterization led to devise a measurement plan in order to test the algorithms' performance in a real scenario. The experimental measurements employed for this test were the result of a collaboration with the group of Prof. Joerg Widmer, Research Director of the institute, and were obtained by exploiting standard 60 GHz hardware. The performance evaluation of the algorithms over experimental data showed that a sub-meter accuracy can be obtained with a low probability of being unable to localize the node.

1.2 THESIS OUTLINE

This thesis is organized as follows. Chapter 2 consists on a review of the state of the art of localization and MMWs: the first Section 2.1 introduces some of the classical localization schemes giving a mathematical explanation and some application examples; the subsequent Section 2.2 is a survey of the recent advances in indoor localization which have been an hint for the development of our localization schemes. Section 2.3 introduces MMWs, analyzes their propagation characteristics in detail, and finally describes related work regarding indoor localization with MMWs. Chapter 3 gives a description of the TV algorithm (Section 3.2), the ADoA algorithm (Section 3.3) and the FP (Section 3.4), explaining how they work with the aid of pseudocodes as well. The following Chapter 4 describes the ray tracer tool we implemented (Section 4.1) and presents a performance evaluation and characterization of the three algorithms (Section 4.2). In Chapter 5, Section 5.1 describes the experimental methodology and the employed hardware we utilized in order to obtain experimental data. The following Section 5.2 presents the performance evaluation of the three algorithms with the collected experimental data. Finally, in Chapter 6 we draw some concluding remarks and devise possible future work and improvements (Section 6.1).

STATE OF THE ART

In this chapter, we survey related work on localization by subdividing the material into a general review of range-based and range-free schemes (Section 2.1), a focus on recent advances in indoor localization (Section 2.2), and a review of multipath-aided localization (Section 2.2.2). Finally we introduce millimeter waves with the related definition, why they are becoming appealing etc., and devise some characteristics of the propagation in indoor environments that may be appealing for localization purposes.

2.1 CLASSIC LOCALIZATION SCHEMES

This section gives a description of the classic schemes exploited for localization purposes. Which one of these methods is preferable depends on the nature of the available information: distances, absolute time, time differences, angles etc. While the procedure to retrieve this kind of data is not specific of each localization scheme, we will also give a brief overview on how the input data required by the schemes can be obtained.

2.1.1 *Trilateration*

Trilateration is a range-based technique which requires the knowledge of the distances d_i between the node to be localized and the ith anchor node located at fixed position $\mathbf{o}_i$. Given a node i located at a point $\mathbf{o}_i = (o_{i,x_1}, o_{i,x_2}, \ldots, o_{i,x_N})$ in a N-dimensional space, the locus of points $\mathbf{p} = (p_{x_1}, p_{x_2}, \ldots, p_{x_N})$ laying at a distance d_i from $\mathbf{o}_i$ is a hypersphere described by the equation

$$(o_{i,x_1} - p_{x_1})^2 + (o_{i,x_2} - p_{x_2})^2 + \cdots + (o_{i,x_N} - p_{x_N})^2 = d_i^2. \qquad (2.1)$$

Defining as M the number of available anchor nodes, the node to be localized satisfies simultaneously M equations like Equation (2.1) related to the ith anchor node's position $\mathbf{o}_i$ and the respective distance from the node to be localized d_i. This leads to a system of M equations in N unknowns:

$$
\begin{cases}
(o_{1,x_1} - p_{x_1})^2 + (o_{1,x_2} - p_{x_2})^2 + \cdots + (o_{1,x_N} - p_{x_N})^2 = d_1^2 \\
(o_{2,x_1} - p_{x_1})^2 + (o_{2,x_2} - p_{x_2})^2 + \cdots + (o_{2,x_N} - p_{x_N})^2 = d_2^2 \\
\qquad\qquad\qquad\qquad\qquad \vdots \\
(o_{M,x_1} - p_{x_1})^2 + (o_{M,x_2} - p_{x_2})^2 + \cdots + (o_{M,x_N} - p_{x_N})^2 = d_M^2
\end{cases}
\tag{2.2}
$$

If the ranges d_i from the anchor points are perfectly known, the system of equations (2.2) admits a unique solution if $M \geq N + 1$. However, if some hyperspheres touch in exactly one point, i. e. there exist some i, j such that $\|\mathbf{o}_i - \mathbf{o}_j\| = d_i + d_j$, less than $N + 1$ equations are required. A graphical example of the system of equations is given in Figure 2.1, where localization is performed in a 2-dimensional environment: the point $\mathbf{p}$ of intersection of the circumferences is the unique point where the distance between anchor nodes' positions $\mathbf{o}_1$, $\mathbf{o}_2$ and $\mathbf{o}_3$ are d_1, d_2 and d_3, respectively.

Since it would be infeasible to directly measure distances, some ranging techniques must be adopted. Thus, the distance will be indirectly inferred from other data.

For example, the GPS, which is based on trilateration, exploits delay measurements to retrieve distances from a constellation of 31 satellites orbiting around the Earth with a revolution period of half a sidereal day and a radius of about $22\,200\,\text{km}$ [12]: in particular, a satellite periodically transmits data frames where a timestamp is attached; a synchronous receiver is then able to measure its distance from the transmitting satellite by measuring the delay experienced by the received frame, by calculating the time difference Δt between its own clock and the frame's timestamp; finally, the distance between the receiver and the satel-
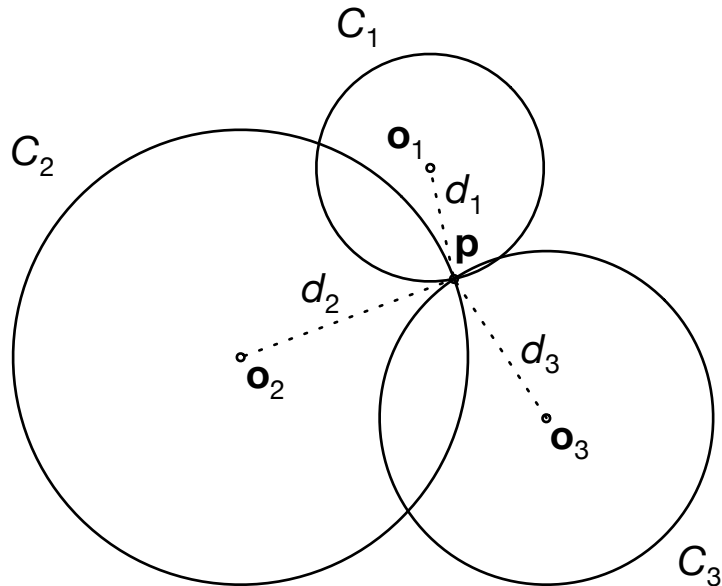
Figure 2.1: Trilateration in a two-dimensional environment ($N = 2$). Except for some limit cases, at least three circumferences are required to obtain a unique intersection.

lite can be calculated as $d = c\Delta t$, where $c = 2.997\,924 \times 10^8 \,\mathrm{ms^{-1}}$ is the speed of light. This ranging technique requires a perfect synchronization between the receiver and the GPS satellite clocks, otherwise delays and thus distance estimates would be biased. An interesting fact is that satellites' clocks exhibit a time drift with respect to a receiver's clock on Earth that needs to be electronically corrected: it is worth noting that the clocks' drift of about $45\,\mathrm{\mu s/day}$ can be estimated through Einstein's Relativity Theory and thus GPS is one example where the theory works [13].

Another ranging technique is Received Signal Strength (RSS) [7]: once an accurate path loss model is provided, the distance can be estimated via received power measurements. One of the simplest models is the free space model provided by the Friis transmission equation which has the form

$$P_L[\mathrm{dB}] = 20 \log_{10} \frac{\lambda}{4\pi d}, \tag{2.3}$$

where P_L is the difference in dB between the transmission power P_{tx} and the received power P_{rx} expressed in dB as well, d is the distance between transmitter and receiver, and λ is the signal wavelength.

Equation (2.3) can be exploited to retrieve d as

$$d = \frac{4\pi}{\lambda} 10^{\frac{P_L}{20}}. \tag{2.4}$$

More complicated models exist in the literature: the simplified path loss model is provided by

$$P_L[\mathrm{dB}] = K[\mathrm{dB}] + 10\gamma \log_{10} \frac{d}{d_0} \tag{2.5}$$

where d_0 is the path loss exponent, d_0 is a reference distance for the antenna's far-field and K is a constant usually assumed equal to the free space path loss calculated at a distance of d_0 from the transmitter. The simple model provides a linear function between the distance and the path loss in dB scale. The simplified model may be exploited to build a more precise multi-slope model to take into account different phenomena that may occur at different distances, e. g. in the two-ray model the path loss slope raises from 20 to 40 dB per decade at a certain distance called the critical distance.

Other models are of empirical nature: an example is the Okumura model [14] which is exploited in large urban macrocells; the model is applicable over distances of 1–100 km and frequency ranges of 150–1500 MHz. Okumura used extensive measurements of base station-to-mobile signal attenuation throughout Tokyo to develop a set of curves giving median attenuation relative to free space of signal propagation in irregular terrain.

2.1.2 *Multilateration*

Multilateration is a localization technique principally based on the Time Difference of Arrival (TDoA) of the signals transmitted by different anchor nodes: time differences can be mapped to distance differences and the geometric locus of points where the difference of distances between two fixed points is an hyperbole.
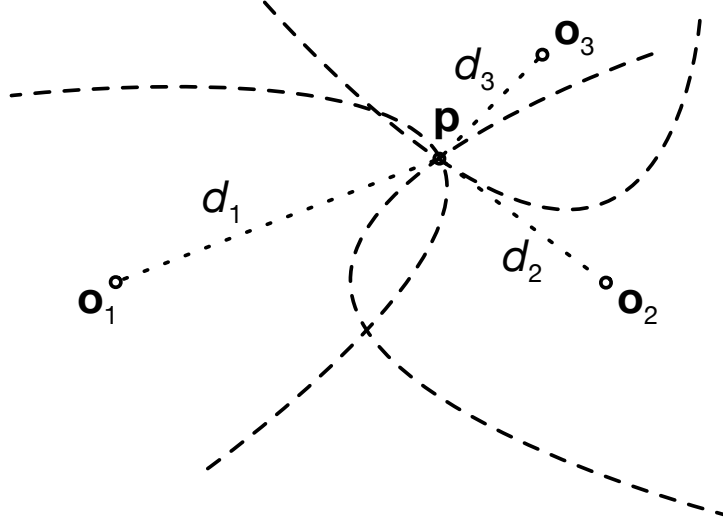
Figure 2.2: Multilateration in a two-dimensional environment ($N = 2$).

Given a point $\mathbf{p} = (p_{x_1}, p_{x_2}, \ldots, p_{x_N})$ in an N-dimensional space, and an anchor node i at position $\mathbf{o}_i = (o_{i,x_1}, o_{i,x_2}, \ldots, o_{i,x_N})$, their distance d_i can be computed as

$$d_i = \sqrt{(o_{i,x_1} - p_{x_1})^2 + (o_{i,x_2} - p_{x_2})^2 + \cdots + (o_{i,x_N} - p_{x_N})^2} \qquad (2.6)$$

which is just Equation (2.1) root-squared.

Given another anchor node $j \neq i$ fixed at position $\mathbf{o}_j$, its distance d_j from the point $\mathbf{p}$ can be calculated according to Equation (2.6). Thus, if $\Delta t_{i,j}$ is the TDoA of signals from i and j, the point $\mathbf{p}$ must satisfy

$$c\Delta t_{i,j} = d_i - d_j \qquad (2.7)$$

where c is the speed of light and d_i and d_j are calculated as before.

Equation (2.7) is the mathematical representation of an hyperbole. If more anchor nodes are available, a set of time differences of arrival can be obtained, leading to a system of equations in the form of Equation (2.7). Possibly, a unique solution exists and this would be the position of the node to be localized.

Note that the exploitation of time differences does not require the node to be localized to synchronize its clock with that of the anchor nodes, which may represent an advantage over trilateration.

The TDoA of a signal can be estimated by two general methods: subtracting Time of Arrival (ToA) measurements from two base stations to produce a relative TDoA, or through the use of cross-correlation techniques, in which the received signal at one base station is correlated with the received signal at another base station.

As an example of a system based on TDoA is Observed Time Difference of Arrival (OTDoA). The system is an optional feature for the localization of mobile terminals in 3GPP LTE networks. The terminology is that used in 3GPP LTE specifications: a User Equipment (UE) is a mobile terminal that has to be localized, and an eNodeB is a base station. The working principles of the system are exactly as explained before: ToAs from several neighboring eNodeBs are subtracted from the ToA of a reference eNodeB to form the OTDoA; geometrically, each ToA determines an hyperbole, and the point at which the hyperboles intersect is the desired UE location. At least three timing measurements from geographically dispersed eNodeBs with good geometry are needed to solve for two coordinates (latitude and longitude) of the UE. A big advantage of OTDoA over simple GPS is that it works indoors or in urban canyons but a disadvantage is that it works poorly in rural areas where the BS density is rather low [15]

2.1.3 *Triangulation*

Triangulation [16] is a technique that relies on angle measurements and thus can be considered range-free. The technique is quite old: in the 6th century BC, the Greek philosopher Thales developed a method based on triangulation in order to calculate the height of the pyramids by measuring the length of their shadows and that of his own at the same moment, and comparing the ratios to his height [17]; anyway there is also evidence that ancient Egyptians were familiar to similar techniques as well. Triangulation is still used in surveying due to its simplicity and
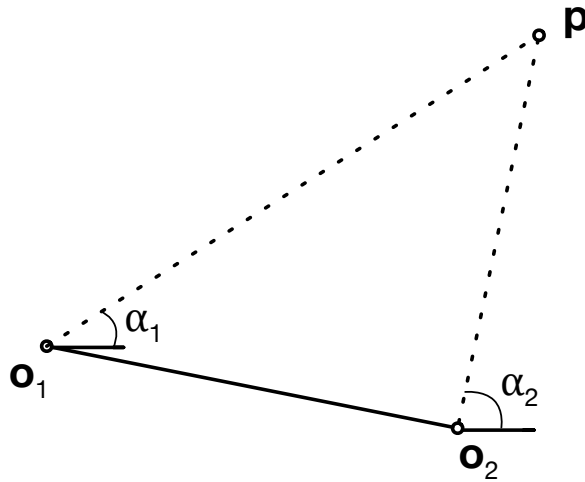
Figure 2.3: A triangulation example.

to the relatively high accuracy provided by theodolites which are utilized for angle measurements; however, applications involving radio frequency signals are also present and are becoming quite popular thanks to the extensive use of antenna arrays and the exploitation of the MUSIC and ESPRIT algorithms [18, 19].

An example of triangulation is represented in Figure 2.3. Here, angles α_1 and α_2 are measured from a common reference half-line, e. g. angles may be referred relatively to a cardinal point; the position of the point **p** may be inferred considering that a triangle is completely determined whenever one side and two angles are known.

Any errors on the estimation of the angles, however, reflect negatively on the accuracy of localization, especially if the distance between the user and the anchor nodes is large. Additionally, triangulation fails if the node is aligned with the anchors because all points on the line connecting the two anchor nodes would be feasible with the measured angles.

2.1.4 *Fingerprinting*

Localization based on location FP [20, 16] relies on the fact that radio waves emitted from one or more anchors yield a practically unique radio "fingerprint" at any given location: such fingerprint can be identified and employed to infer the location itself.

A localization system based on FP requires a preliminary training phase (or offline stage) where fingerprints at known locations are collected. In this way, a fingerprint database is constructed. The training phase is opposed to the positioning phase (or online stage) where, after some measurements, a node to be localized builds a fingerprint and attempts to localize via a positioning technique relying on the fingerprint database built in the training phase. Usually fingerprints are represented as vectors of some measured quantities such as RSS and time delays, and the positioning technique may exploit a probabilistic framework like a Maximum Likelihood (ML) estimator, or a deterministic procedure, such as a simple closest vector lookup or a more sophisticated algorithm like the k-nearest-neighbor (kNN) [16].

Anyway, while the definitions of fingerprint may vary widely depending on the scenario and radio technology employed, the approach per se is often dismissed due to the heavy preliminary measurements required to construct a fingerprint database, and to the strong dependence of the localization error on the number of fingerprint measurements. However, recent work has revived FP by suggesting that the database construction task can be crowdsourced [21].

2.2 RECENT ADVANCES IN INDOOR LOCALIZATION

2.2.1 *Developed frameworks and systems*

In this section we review some of the newest techniques adopted for indoor localization. Recent work reconsidered WiFi-based indoor localization. The authors

in [22] develop and implement an indoor localization system called ArrayTrack. The system relies on the capabilities of MIMO systems to detect Angle of Arrival (AoA) of incoming signals: a mobile terminal transmits some frames that will be received by one or more AP equipped with MIMO technologies; thus, each AP will be able to detect the AoA and RSS of the signal from the mobile terminal, and build a so-called AoA spectrum, which represents the received power as a function of the pointing angle; AoA spectra at the APs are processed in order to suppress multipath components; finally, a central server processes the data from the APs and calculates the mobile terminal position through localization and trilateration techniques. The system has been implemented by the same authors and they obtained a sub-meter error exploiting six APs in an office environment and with a latency of about 100 ms.

Authors in [23] have developed a similar system like ArrayTrack and named CU-PID. It utilizes PHYsical layer (PHY) information to extract the signal strength and the angle of only the direct path, successfully avoiding the effect of multi-path reflections. Moreover, CUPID is able to localize a device when only a single APs is present. When a few more APs are available, the implemented system can improve the median localization error to 2.7 m.

Another framework has been developed in [24]: the developed system, named Centaur, is able to localize portable devices exploiting Radio Frequency and Acoustic Ranging measurements and Bayesian inference. A further contribution by the same authors is EchoBeep, a technique to enhance Acoustic Ranging in the presence of non-line-of-sight signals.

In [25] the authors develop a localization system exploiting only one AP, and where part of the complexity of the scheme is delegated to the user to be localized, which is assumed to know his own orientation in space, and the distance covered while moving, thanks to the use of a digital gyroscope and accelerometer.

The authors of [26] developed a protocol for ranging measurements in ad hoc WiFi networks that does not rely on synchronization between the nodes, but rather on the estimation of the round trip times. The possible presence of non-line-of-sight components that may alter Time of Flight measurements is filtered

at the receivers by using the MUltiple SIgnal Classification (MUSIC) algorithm which permits to detect the LoS component and to base the measurements on that.

2.2.2 *Multipath-aided localization in UWB channels*

In this section we survey the work by Meissner *et al.* from the University of Graz, Austria, which deserves a separate section because some ideas developed in their research were the starting point for our work.

The work of the authors is principally based on Ultra Wide Band (UWB) signals. A channel model for this type of signals can be found in [27]. As stated in the same paper, the very short time duration (and the relatively high bandwidth) of UWB pulses makes them a good choice for indoor localization due to the possibility to distinguish different MultiPath Components (MPCs) in the estimated Channel Impulse Response (CIR). Thus, UWB pulses can be exploited to collect ToA/TDoA information. This leads to what is referred to as multipath-aided localization, a scheme suitable to localize mobile terminals with the aid of only one AP and of the MPCs resulting from the reflections of the AP signals in the surrounding environment.

In [28], localization is performed by exploiting a ML estimator for the position with the aid of a single AP and the knowledge of the floor plan. It is assumed that the AP transmits UWB pulses periodically: this allows a receiver at an unknown position to determine the CIR which, typically, contains LoS and NLoS components that are separable due to the nature of UWB transmission. The obtained CIR is then exploited in order to determine ToA and therefore ranging information about the various MPCs. The intuition of the authors is that each MPC can be directly mapped to a Virtual Anchor (VA) from where the signal propagates directly to the node, i. e. a straight line without reflections connects the VA and the node to be localized. The VAs are found as the mirrored instances of the unique physical anchor node over the room obstacles, e. g. walls, doors, tables etc., and their position can be determined assuming the knowledge of
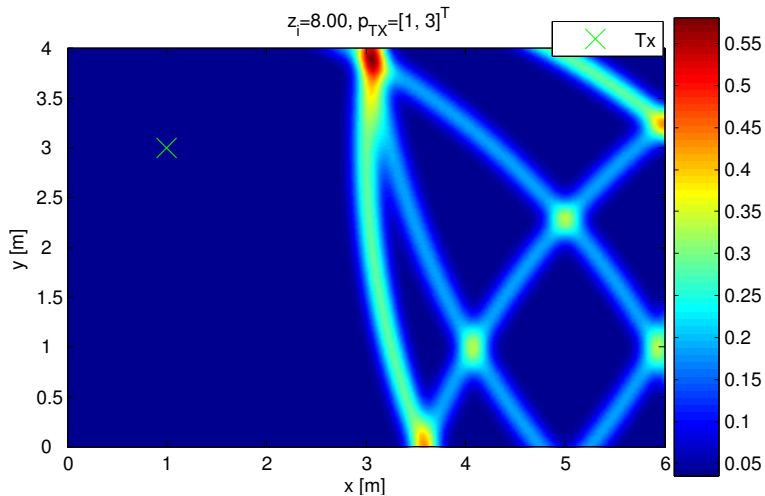
Figure 2.4: Graphical representation of the likelihood function of the node to be local-
ized as a function of the determined ranges. Red areas indicate that the
node is very likely located at the corresponding positions. (Image taken
from [28].)

the floor plan and the anchor node position. Thus, given the obtained set of
ranges, localization is performed by building a likelihood function which returns
the probability of observing the set of inferred ranges as a function of a given
position inside the room and the disposition of the anchor nodes. Figure 2.4 is
taken from [28], and graphically represents the likelihood function obtained over
the points of the floor plan. The areas in red are the positions where it is more
likely the node is located.

In [29, 30], the same authors perform the localization of a moving agent exploit-
ing the correlation in successive positions using state-space concepts as a Kalman
Filter (KF) and a PF. The authors achieved an accuracy of about $45\,\mathrm{cm}$ for $90\,\%$
of the position estimates in a typical pedestrian motion scenario. In particular,
Figure 2.5 represents the track estimates computed via a PF: the route begins in
the upper-left corner, and the only substantial errors are at the beginning, and
are mostly due to non-perfect initialization.

The later work [31] shows as, most of the times, the deterministic multipath
component is a predominant part, in terms of energy capture, of the UWB CIR
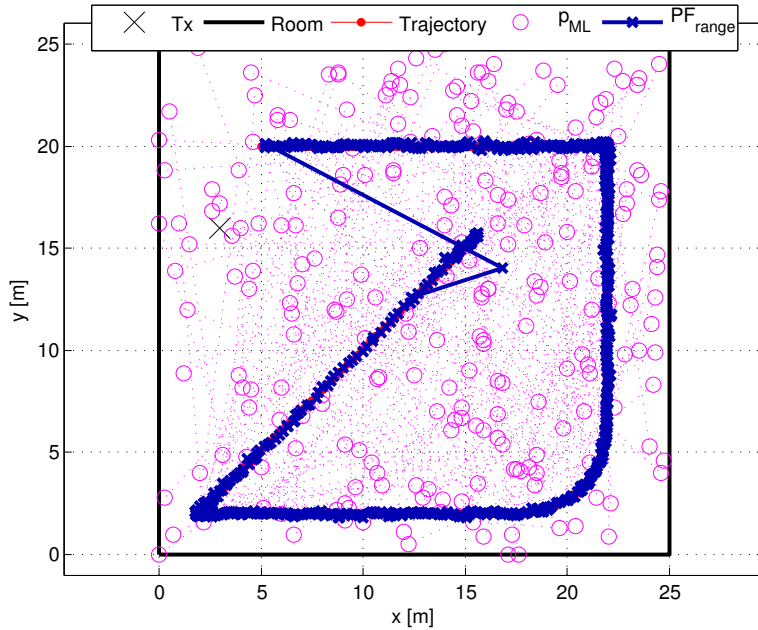
Figure 2.5: Tracking estimates obtained with a Particle Filter (PF). (Image taken from [29].)

(up to a 90 %): this justifies the approach in [28] of considering valid the VAs and the perfect reflections of the signal from the unique AP.

In [32], the authors formalize all the previous work introducing Multipath-assisted indoor navigation and tracking (MINT) and extend the scenario to multiple anchors. Also, they improve the localization method: they introduce two ranging algorithms, ML and Jump-Back Search-Forward (JBSF), and an Extended Kalman Filter (EKF) for localization purposes which requires a scheme for Data Association (DA) that permits to associate range measurements to corresponding VAs.

Finally, along the same lines of [33], in [34] the authors obtain a performance bound for the latter localization scheme MINT, deriving Fisher Information Matrixes (FIMs) and Position Error Bounds (PEBs).

2.3 MILLIMETER WAVES AND LOCALIZATION ALGORITHMS.

2.3.1 *Millimeter waves' definition and challenges*

The International Telecommunication Union (ITU) proposed that the radio spectrum shall be subdivided into nine frequency bands, which shall be designated by progressive whole numbers [1]. The band designated as Extremely High Frequency (EHF) has a frequency range that spans from 30 to 300 GHz. The related wavelengths, that can be easily calculated assuming $\lambda = c/f$ go from 1 mm to 10 mm, and thus the name millimeter waves or millimetric waves to designate signals belonging to the EHF band.

Band number	Symbols	Frequency range (lower limit exclusive, upper limit inclusive)	Corresponding metric subdivision	Metric abbreviations for the bands
3	ULF	300-3 000 Hz	Hectokilometric waves	B.hkm
4	VLF	3-30 kHz	Myriametric waves	B.Mam
5	LF	30-300 kHz	Kilometric waves	B.km
6	MF	300-3 000 kHz	Hectometric waves	B.hm
7	HF	3-30 MHz	Decametric waves	B.dam
8	VHF	30-300 MHz	Metric waves	B.m
9	UHF	300-3 000 MHz	Decimetric waves	B.dm
10	SHF	3-30 GHz	Centimetric waves	B.cm
11	EHF	30-300 GHz	Millimetric waves	B.mm
12		300-3 000 GHz	Decimillimetric waves	B.dmm
13		3-30 THz	Centimillimetric waves	B.cmm
14		30-300 THz	Micrometic waves	B.μm
15		300-3 000 THz	Decimicrometric waves	B.dμm

Figure 2.6: The spectrum subdivision proposed by the ITU. (Image taken from [1].)

The first documented work about millimeter waves belongs to the Indian physicist Jagadish Chandra Bose (1858 - 1937) [35]: the scientist built a rudimentary machinery made of circular waveguides, horn antennas and semiconductors junctions (Bose has also been awarded with the world's first patent for a semiconductor), and performed experiments with radio waves of length ranging from 2.5 cm to 5 mm; as a botanist, he also studied effects of electromagnetic pollution,
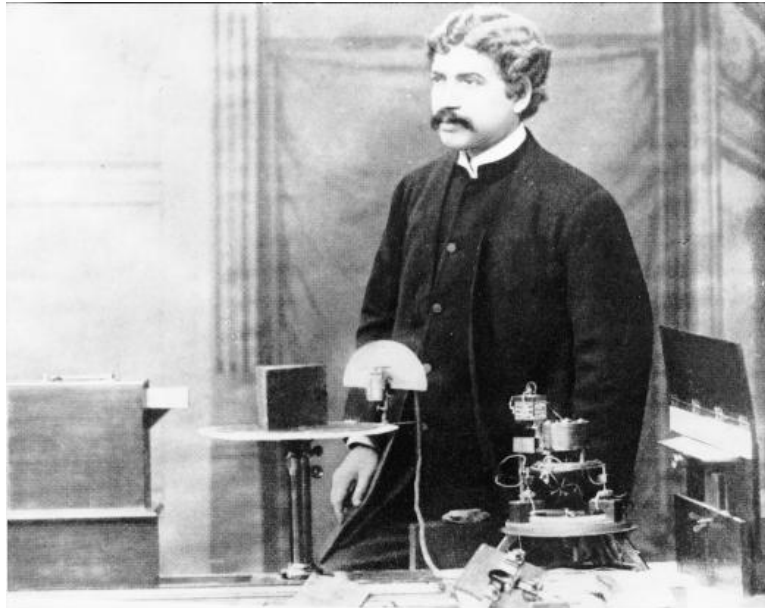
Figure 2.7: The pioner of millimeter waves J.C. Bose at the Royal Institution, London, 1897. (Image taken from [35].)

in particular on plant growth; last but not least, in 1895 he had demonstrated publicly remote signalling by wireless some two years before Marconi's famous Salisbury Plain demonstration of 1897; however, the results he obtained were only considered after his death.

Nowadays, besides military and medical applications where they are extensively used, millimeter waves are becoming appealing because it has become apparent that there is a need for more bandwidth to support new communication services for mobile users [4, 36]. With the current bandwidth allocation in the microwave (µW) frequency range (in the ITU classification, microwaves belong to the Super High Frequency (SHF) band ranging from 3 to 30 GHz), it is very difficult to provide such a system capacity increase without incurring in massive costs due to the extreme densification of the cellular infrastructure. However, recent studies on the propagation characteristics of millimeter wave, as well as advances in the design of Radio Frequency (RF) circuits at those frequencies, have shown that using MMW bands for 5G cellular is actually feasible, and has the potential to solve the spectrum crunch thanks to the huge amounts of bandwidth available [4, 3, 2].

Along the lines of the research for transmission systems, there is a need to study localization schemes that would be suitable and designed to exploit the propagation characteristics of millimeter waves. The following Section 2.3.2 is reviews the propagation characteristics of millimeter waves; then, Section 2.3.3 surveys related work on localization achieved by exploiting millimeter waves.

2.3.2 *Propagation characteristics of millimeter waves*

The radio propagation characteristics at millimeter wave frequencies are starkly different from their µW counterparts. First, according to the free space path loss derived by the Friis transmission equation (see Equation (2.3)), the path loss can easily exhibit 30–40 dB more attenuation because of the smaller wavelength. Moreover, besides free space path loss, compared to lower bands, EHF radio waves have high atmospheric attenuation, being absorbed by the gases in the atmosphere. In particular, as it is possible to see in Figure 2.8, signals in the 57–64 GHz region are subject to the resonance of oxygen molecules and are thus severely attenuated. Also, even over relatively short distances, rain fade is a serious problem, caused when absorption by rain reduces signal strength. In climates other than deserts absorption due to humidity also has an impact on propagation.

Thus, the high path loss experienced by millimeter waves restricts their usage for terrestrial communication up to a distance of about a kilometer and necessitates the use of fairly narrow and very directional es in order to obtain higher power in reception. This can be realized through phased antenna arrays, whose implementation within a reasonable amount of space is made possible thanks to the smaller wavelengths that correspond to these frequencies. All this may seem a limiting fact and a disadvantage for millimeter waves, but, from a networking perspective, it allows to confine signals (for example, making it possible ot limit the coverage area of a private wireless network), and also permits smaller frequency reuse distances than possible at lower frequencies, granting higher achievable capacities. Moreover, the short wavelength makes it possible to pack a large number of antennas in a relatively small space. This means that both standard and mas-
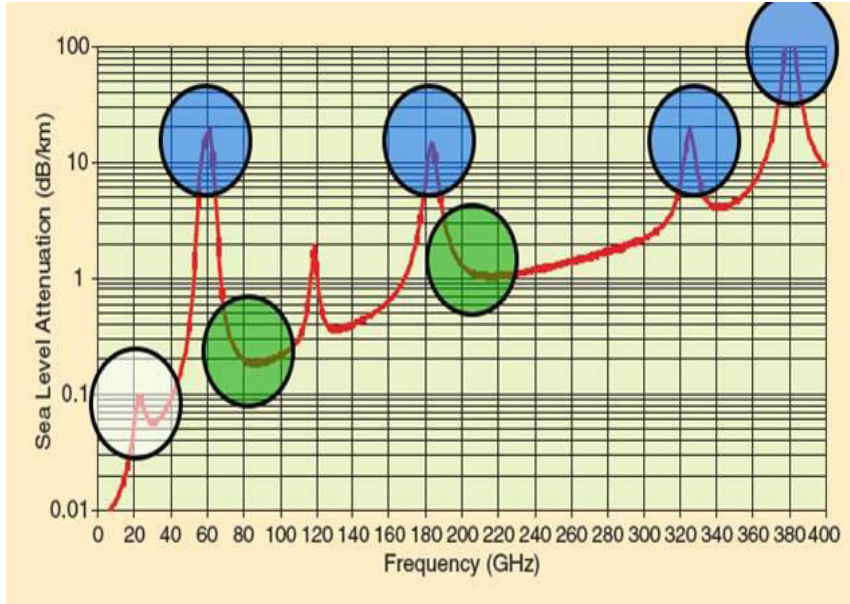
Figure 2.8: The sea level attenuation in dB/km experienced by millimeter waves as a function of frequency. Attenuation exhibits a non-linear behavior (in the logarithmic domain) due to physical phenomena such as the oxygen resonance at 60 GHz. (Image taken from [2].)

sive MIMO approaches become feasible [37], further increasing frequency reuse potential.

The expected use of directive antennas implies the necessity of further studies regarding millimeter waves propagation in environments where significant reflections may originate from the environment boundaries. The following paragraph describes the scattering and the behavior of millimeter waves when bouncing off obstacles.

The paper[38] presents a model for the Power Delay Profile (PDP) perceived by a receiver at a fixed position in a rectangular room with a unique transmitter: with an argument based on ellipsoids, the authors obtain an integral form for the power value of each delay in the PDP. The model resulted to fit well the experimental data.

Some experiments to model the scattering of millimeter waves have been carried out in [39] but with special regard to outdoor surfaces such as roads; some further experiments can be found in [40], where radiative transfer theory is exploited. A

brief overview of the theory can be found in [41]. An exhaustive modeling of the scattering is presented in [42], where the authors distinguish between two scattering components: volume and surface scattering. For the purposes of this thesis, such a model factors in an excessive number of details: as it will be clearer later, we are mostly concerned in the quasi-optical nature of millimeter waves.

In [43], the authors performed some measurements about reflections of MMW beams and obtained characteristic scattering patterns. Aiming to build a simulator, they interpreted the deterministic patterns as probability radiation patterns: given a directive beam bouncing off a wall, a unique reflected beam is expected and its direction is randomly chosen with a probability determined by the amplitude of the deterministic radiation pattern, i.e. the most probable directions are those where the power is concentrated in the deterministic pattern . For instance, the most probable direction is that predicted by Snell's equation which states that the reflected wave has the same incidence angle of the incidence wave. The simulation results obtained resulted to be enhanced with the exploitation of the probability radiation patterns.

Another study involving radiation patter measurements is in [44], where radiation patterns are called power angle profiles Power Amplitude Profiles (PAPs). The experiments conducted in this work regarded 60 GHz millimeter waves, and were conducted in different office environments: one of the main assumptions is that millimeter waves PAPs have a negligible probabilistic component due to scattering, i.e., directions with the highest received power are those determined by rays that incurred in perfect reflections. Thus, millimeter waves have a quasi-optical behavior. A similar statement can be found in [11]. The quasi-optical behavior has also been proved relatively to lighting models, generally used in computer graphics: the authors in [45] present a set of measured reflection patterns and compare them to two models, by Lambert and Phong respectively; a further study in [46] presents a modified Phong's model for radar applications and in its conclusions new sophisticated models are indicated such as Blinn-Phong model and Schlick's model. In all these models the deterministic reflection dominates over the scattering component.

2.3.3 *Localization schemes exploiting millimeter waves*

In the literature there exists a scarce amount of material regarding localization exploiting the peculiar characteristics of millimeter waves and, as has been said in Chapter 1, this is one of the motivations of our work. The following is a short survey of the state of the art regarding localization with millimeter waves.

Authors in [47] evaluate performance of RSS-, TDoA- and AoA-based localization schemes assuming the presence of several anchor nodes deployed over a circumference around the receiver. It is observed that the AoA approach achieves the smallest localization error because of the broad AoA spectrum diversity originating from the circular geometry of the anchor nodes deployment.

In [48], a method is developed for the estimation of the TDoA based on the interference between Orthogonal Frequency Division Multiplexing (OFDM) symbols from two different transmitters. The technique makes it possible to leverage actual data communications for location estimation, without having to rely on a different, specific protocol.

In [49], the authors exploit Differential Time Difference of Arrival (DTDoA), an improved version of TDoA, which does not require synchronization between the anchor nodes. Time information is extracted from the 60 GHz OFDM transmission frames exchanged by the node to be localized and, at least, 4 anchor nodes. The localization error of the developed system has been investigated, and showed a median of about 1 m.

Exploiting MIMO techniques for millimeter waves lead to a sparse representation of the MIMO channel matrix [10]. This is a peculiar characteristic of MMWs, and, leveraging on this, the authors in [50] developed a localization scheme based on sparse beamspace channel signatures where LoS information is not mandatory and where the room plan is subdivided into cells; then, given the sparse representation of the channel matrix at the unknown position obtained via measurements possibly affected by noise, a ML estimator returns the position associated to the most likely cell. Performance evaluation is carried out in terms of error probability that a user localizes itself in a cell different from the one where it is placed.

Anyway, this probability has been shown that cannot be made arbitrarily small for a fixed cell size: for a $25 \times 25\,\mathrm{m}^2$ cell, the probability is about $4\,\%$, whereas for a $5 \times 5\,\mathrm{m}^2$ it is about $6\,\%$.

The last presented work may appear promising, but it has to be noticed that the introduced error probability decreases as long as the cell dimension increases, but if a small localization error is sought, the cell size must be decreased. The other presented material relies on classical localization schemes that do not exploit the particular characteristic of MMWs. For example, MMW communications must rely on highly directive antennas: none of the methods seems to exploit this feature. Instead, highly directive antenna patterns may be exploited in conjunction with the fact that MMWs propagation is quasi-optical [44, 11]. Moreover, MPCs are usually seen as a sort of interference that needs to be filtered out: instead, we claim that, as per [28], MPCs may be exploited too, enabling a localization scheme which relies on a unique AP, and this is the motivation behind our work. In the next chapter, we discuss how MMW propagation properties have been factored in to design three different localization algorithms.

MILLIMETER WAVE LOCALIZATION SCHEMES

This chapter describes the three MMW localization algorithms devised in this work of thesis. The first paragraphs are a description of the localization scenario and introduce the symbols used throughout the thesis.

The indoor localization scenario for the three developed algorithm is a room bounded by walls, a ceiling and a floor. With the notation introduced in Section 2.1, let $N = 3$, i.e. we assume a 3D space. Without loss of generality, we introduce a rectangular room scenario where we set a three-dimensional Cartesian coordinates system to be centered in one of the corners of the room. The coordinates system introduces the three canonical vectors of the three axes $\mathbf{e}_x = (1, 0, 0)$, $\mathbf{e}_y = (0, 1, 0)$ (oriented orthogonally along the floor sides), and $\mathbf{e}_z = (0, 0, 1)$ (oriented along the height of the room). Any point $\mathbf{q} = q_x \mathbf{e}_x + q_y \mathbf{e}_y + q_z \mathbf{e}_z$ is a linear combination of the three canonical vectors and can be mapped to a triple (q_x, q_y, q_z).

The room boundaries and any other obstacles containing radio-reflective surfaces are grouped in the reflective objects set $\mathcal{Z}$. Obstacles in the set $\mathcal{Z}$ are represented as three-dimensional polyhedra with flat polygonal faces, straight edges and sharp vertices. We treat each obstacle's face as an oriented surface S, represented by its normal vector $\mathbf{n}$, which, given three different points of the surface $\mathbf{p}_1$, $\mathbf{p}_2$ and $\mathbf{p}_3$, can be found as

$$\mathbf{n} = \frac{(\mathbf{p}_2 - \mathbf{p}_1) \times (\mathbf{p}_3 - \mathbf{p}_1)}{\|(\mathbf{p}_2 - \mathbf{p}_1) \times (\mathbf{p}_3 - \mathbf{p}_1)\|} . \tag{3.1}$$

The operator $\| \cdot \|$ denotes the Euclidean norm, and $\times$ the cross-product.

We assume that a single MMW AP is installed in the room at the location $\mathbf{p}_{\text{TX}}$ and is employed as an anchor node for localization purposes. The algorithms are designed to leverage on direct signals from the AP and on the reflections off indoor boundaries in order to compute location estimates. The input to all

algorithms is the AoA spectrum $P_{\mathbf{p}}(\alpha)$, which records the distribution, over the azimuthal plane, of the amplitude of multipath components at a given location $\mathbf{p}$, as a function of the azimuth ϕ, assumed to be measured relative to a reference direction ϕ_0 in the Cartesian coordinate system. Since the AoA spectrum is only referred to the azimuthal plane, the localization returns an estimate in the same plane, i.e., two-dimensional localization is performed and no height information is revealed. The availability of the only azimuthal AoA spectra was determined by the available hardware for the experimental evaluation of the algorithms, but if three-dimensional AoA spectra would be available, the same algorithms can be straightforwardly extended to the 3D localization case.

The AoA spectrum $P_{\mathbf{p}}(\phi)$ is processed by the algorithms to yield a compact representation of different MPCs at $\mathbf{p}$. In particular, the AoA spectrum is initially smoothed in order to filter possible present noise: for example, this may be the case of an experimentally measured AoA spectrum). Then a peak on the reception pattern is identified with an MPC [44]. Note that an MPC can be either a LoS path or a path that incurred (possibly multiple) reflections off one or more surfaces of the elements in $\mathcal{Z}$. The detected MPCs are collected in a $2 \times N_{\mathbf{p}}$ matrix $\mathbf{M}^{(\mathbf{p})}$, where $N_{\mathbf{p}}$ is the number of detected MPCs in $P_{\mathbf{p}}(\alpha)$. The first row of $\mathbf{M}^{(\mathbf{p})}$ contains the amplitude of each MPCs sorted in decreasing order; the second row contains the AoA of the MPC, relative to ϕ_0. In this way, each column $\mathbf{M}^{(\mathbf{p})}_{:,k}$ of $\mathbf{M}^{(\mathbf{p})}$ (where the semicolon notation $_{:,k}$ denotes all elements of the corresponding dimension, and in this case it means all rows of column k) can be seen as a vector in polar coordinates, departing from $\mathbf{p}$, where $\mathbf{M}^{(\mathbf{p})}_{1,k}$ and $\mathbf{M}^{(\mathbf{p})}_{2,k}$ denote the amplitude and phase of the vector relative to ϕ_0, respectively.

We also assume that the room geometry (i.e., $\mathbf{p}_{\mathrm{TX}}$ and $\mathcal{Z}$) is treated as inputs for the algorithms.

3.1 VIRTUAL ANCHOR NODES

In this preliminary section, we provide more precise definitions about Virtual Anchor (VA) anchor nodes, which will be required by the algorithms in Section 3.2 and Section 3.3.

Each MPC belonging to the AoA spectrum $P_{\mathbf{p}}(\alpha)$ perceived at location $\mathbf{p}$ can be modeled as emitted by a VA node that would be the source of a LoS signal reaching $\mathbf{p}$ along the same AoA of the MPC. The position of the VA can be determined by mirroring the position of the AP with respect to the surfaces the signal has reflected off.

Call $\mathcal{A} = \{\mathbf{a}_0, \mathbf{a}_1, \dots\}$ the set containing the positions of the possible VAs, and call $\bar{\mathcal{A}} = \{A_0, A_1, A_2, \dots\}$ a partition of this set. We let $A_0 = \mathbf{p}_{\text{TX}}$, whereas each set A_i, $i = 1, 2, \dots$ contains the VAs that have been mirrored i times with respect to any surface of the objects in $\mathcal{Z}$, i.e. A_i contains the virtual anchor nodes that may generate direct signals that otherwise would have incurred in i reflections in the environment. Note that $\mathcal{A}$ and $\bar{\mathcal{A}}$ have countably infinite cardinality, as there is no limit to the number of times the AP can be mirrored. However, in practice the MMW signals from the AP will fade quickly as they propagate and reflect off surfaces, a substantially different aspect with respect to, e.g., UWB systems at lower frequencies. Therefore, it makes sense to truncate $\mathcal{A}$ by considering a maximum reflection order μ [44]. To this end, we define $\mathcal{A}_\mu = \bigcup_{i=0}^{\mu} A_i$.

Figure 3.1 shows two VAs $\mathbf{a}_i$ and $\mathbf{a}_j$ corresponding to a first- and a second-order reflection, respectively. The node $\mathbf{a}_i$ is found by mirroring $\mathbf{p}_{\text{TX}}$ over the vertical line representing a wall and it would be a source of first order reflections, i.e. $\mathbf{a}_i \in A_1$. Then, the node $\mathbf{a}_j \in A_2$ is found by mirroring $\mathbf{a}_i$, which belongs to A_1, over then horizontal line (mirroring again over the vertical line returns again $\mathbf{p}_{\text{TX}}$ but this is avoided in Line 11). It is now clear as the rays arriving at $\mathbf{p}$ and transmitted by the unique AP in the room, can be seen as directly coming from anchor nodes of different reflection order.

The recursive algorithm with pseudo-code given in Algorithm 1 explains how to populate the sets A_i of the partition of $\mathcal{A}$ given the desired reflection order i,
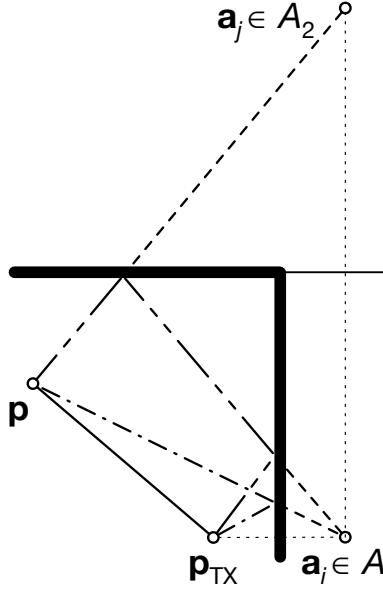
Figure 3.1: Virtual anchor nodes related to first- and second-order reflections.

and the inputs $\mathbf{p}_{\text{tx}}$ and $\mathcal{Z}$. The algorithm is recursive since in Line 4 the algorithm itself is called, with a reflection order decreased by 1. Recursive calls end when $i = 0$ and the AP position $\mathbf{p}_{\text{TX}}$ is returned (Line 2): a reflection order $\mu = 0$ means that only direct paths and they can only be provided by the AP. Then, the set A_i is populated by processing each element in A_{i-1} (Line 6) and by calculating its mirrored instance over every surface of any obstacle element in $\mathcal{Z}$ (Lines 7-9). In particular, Line 9 computes the mirrored replica $\bar{\mathbf{p}}$ of a point $\mathbf{p}$ based on the normal vector $\mathbf{n}$ describing a surface S as

$$\bar{\mathbf{p}} = \mathbf{p} - 2\mathbf{n} \cdot (\mathbf{p} - \mathbf{q}) \, , \tag{3.2}$$

where $\cdot$ denotes the dot product, and $\mathbf{q} \neq \mathbf{p}$ is any point of S. Finally, duplicates and anchor nodes that may belong to anchor nodes sets with lower index are not included in A_i as per Lines 10 and 11.

Still referring to Figure 3.1, if we want to detect second order VAs ($\mu = 2$) such as the one at position $\mathbf{a}_j \in A_2$, Algorithm 1 would recall itself in order to detect first order VAs ($\mu = 1$): given $\mathbf{a}_i \in A_1$ (that can be found by mirroring

---

Algorithm 1: Construction of the set A_i.

---

1 **Function** DETERMINEANCHORS *(i, $\mathbf{p}_{\mathrm{TX}}$, $\mathcal{Z}$)*

2   **if** $i = 0$ **then return** $\{\mathbf{p}_{\mathrm{TX}}\}$

3   **else**

4 $A_{i-1} \leftarrow$ DETERMINEANCHORS$(i-1, \mathbf{p}_{\mathrm{TX}}, \mathcal{Z})$

5 $A_i \leftarrow \varnothing$

6   **foreach** *anchor node* $\mathbf{a} \in A_{i-1}$ **do**

7   **foreach** *obstacle* $z \in \mathcal{Z}$ **do**

8   **foreach** *surface* S *of* z **do**

9 $\bar{\mathbf{a}} \leftarrow$ mirror $\mathbf{a}$ over S using (3.2)

10   **if** $\bar{\mathbf{a}} \notin A_i$ **then** $A_i \leftarrow A_i \cup \{\bar{\mathbf{a}}\}$

11   **return** $A_i \setminus (\{\mathbf{p}_{\mathrm{TX}}\} \cup A_{i-1})$

---

the unique anchor node of $\mu = 0$, i.e. the AP at position $\mathbf{p}_{\mathrm{TX}}$, over the vertical line) $\mathbf{a}_j$ is found by mirroring $\mathbf{a}_i$ over the horizontal line.

3.2 THE TRIANGULATE-VALIDATE (TV) ALGORITHM

The first algorithm we present permits a node at an unknown position $\mathbf{p}$ to estimate its position via a number of triangulation steps followed by a validation of the estimated locations, and thus the name TV. The algorithm assumes that the node has measured the AoA spectrum $P_{\mathbf{p}}(\alpha)$ and has derived the matrix $\mathbf{M}^{(\mathbf{p})}$ described previously. We assume the knowledge of the transmitter position $\mathbf{p}_{\mathrm{TX}}$, the set of obstacles $\mathcal{Z}$, that may model walls and boundaries, and the reference direction ϕ_0 from where angles are measured.

If the association between the anchors in $\mathcal{A}$ and the MPCs in $\mathbf{M}^{(\mathbf{p})}$ were known, it would be possible to directly triangulate the position of $\mathbf{p}$, and this would be a relatively simple problem. However, such association is unknown, leading to a higher complexity: the algorithm that follows is designed to solve the localization problem with a procedure less complex than the reformulation of the ML approach in [28] to employ AoA information (in [28], the information was related to distances from the VAs).

With reference to the pseudo-code in Algorithm 2, we start by considering VAs up to a given reflection order μ. While a high value of μ would yield a richer virtual anchor set $\mathcal{A}_\mu$, a low value is more meaningful for triangulation: in fact, reflections weaken the signal, and VAs of higher order can be quite far from the receiver, and this distance would translate into a large triangulation error in the presence even of only small errors in the AoA spectrum. In addition, a signal at MMW frequencies is rarely distinguishable from noise after more than two reflections, hence we set $\mu = 2$ in the following.

We start by considering $\mathbf{M}_{:,1}^{(\mathbf{p})}$ and $\mathbf{M}_{:,2}^{(\mathbf{p})}$ which, due to the sorting of $\mathbf{M}^{(\mathbf{p})}$, correspond to the MPCs with highest amplitude. Before using them to triangulate a position, we need to transform these entries into vectors *departing* from the position of any anchor, expressed relative to the reference Cartesian coordinates system of the room. This yields two vectors $\mathbf{u}_1 = -\mathbf{Q}\mathbf{M}_{:,1}^{(\mathbf{p})}$ and $\mathbf{u}_2 = -\mathbf{Q}\mathbf{M}_{:,2}^{(\mathbf{p})}$, where $\mathbf{Q}$ is the coordinates transformation matrix (Line 3). We now make an initial guess that the anchors from which $\mathbf{u}_1$ and $\mathbf{u}_2$ emanate are two points $\mathbf{a}_i, \mathbf{a}_j \in \mathcal{A}_\mu$ and triangulate a location over the azimuthal plane by solving the following linear system in two unknowns $t_1 \geq 0$ and $t_2 \geq 0$ (Line 6):

$$\mathbf{a}_i + \mathbf{u}_1 t_1 = \mathbf{a}_j + \mathbf{u}_2 t_2 \ . \tag{3.3}$$

Triangulating with the directions of the strongest MPCs guarantees a sort of noise filtering of the AoA spectrum $P_{\mathbf{p}}(\alpha)$. Call $\mathbf{p}_k$, $k \geq 0$ the position found. If $\mathbf{p}_k$ is valid with respect to some logical constraints (e.g., it is inside the room, not within any of the obstacles in $\mathcal{Z}$, and does not coincide with $\mathbf{p}_{\text{TX}}$, Line 7), we validate the position by basically measuring how compatible the remaining MPCs are with the positions of other VAs in $\mathcal{A}_\mu$. We assign a weight $w_k > w_\ell$ to all anchors of partition subsets A_k and A_ℓ, $0 \leq \ell < k \leq \mu$, $A_k, A_\ell \subset \mathcal{A}_\mu$. This reflects the fact that the validation involving VAs closer to $\mathbf{p}$ should be given greater importance. We now choose $\mathrm{v}_{\max}$ further MPCs $\mathbf{M}_{:,m}^{(\mathbf{p})}$, $3 \leq m \leq \mathrm{v}_{\max} + 2$,

---

Algorithm 2: The Triangulate-Validate algorithm.

1 Function TRIANGVAL $(P_{\mathbf{p}}(\alpha),\ \mathbf{p}_{\text{TX}},\ \mathcal{Z},\ \phi_0,\ \mu,\ \text{v}_{\max})$

2      $\mathcal{A}_\mu \leftarrow \bigcup_{\ell=0}^{\mu} \text{DETERMINEANCHORS}(\ell, \mathbf{p}_{\text{TX}}, \mathcal{Z})$

3   Map $\mathbf{M}^{(\mathbf{p})}$ to canonical base, compute $\mathbf{u}_1$, $\mathbf{u}_2$

4      $k \leftarrow 0$

5   **foreach** *pair* $(\mathbf{a}_i, \mathbf{a}_j), \mathbf{a}_i, \mathbf{a}_j \in \mathcal{A}_\mu, i \neq j$ **do**

6          $\mathbf{p}_k \leftarrow$ point such that $\mathbf{a}_i + \mathbf{u}_1 t_1 = \mathbf{a}_j + \mathbf{u}_2 t_2$

7   **if** ISVALID$(\mathbf{p}_k, \mathcal{Z})$ **then**

8              $\mathcal{T} \leftarrow \mathcal{A}_\mu \setminus \{\mathbf{a}_i, \mathbf{a}_j\}$

9              $c_k \leftarrow 0$

10   **for** $m = 3$ **to** $\text{v}_{\max} + 2$ **do**

11                 $\mathbf{u}_m \leftarrow -\mathbf{Q}\mathbf{M}^{(\mathbf{p})}_{:,m}$

12                 $c_k \leftarrow c_k + \min_{\mathbf{a} \in \mathcal{T}} \text{COST}(\mathbf{p}_k, \mathbf{a}, \mathbf{u}_m)$

13                 $\mathcal{T} \leftarrow \mathcal{T} \setminus \{\arg\min_{\mathbf{a} \in \mathcal{T}} \text{COST}(\mathbf{p}_k, \mathbf{a}, \mathbf{u}_m)\}$

14             $k \leftarrow k + 1$

15   **return** $\hat{\mathbf{p}} = \sum_{k=1}^{K} c_k^{-1} \mathbf{p}_k / \sum_{k=1}^{K} c_k^{-1}$

---

to be involved in the validation process. For each MPC, we consider all VAs in $\mathcal{T} = \mathcal{A}_\mu \setminus \{\mathbf{a}_i, \mathbf{a}_j\}$ and associate a cost c_k to $\mathbf{p}_k$ as follows:

$$c_k = \sum_{m=3}^{\text{v}_{\max}+2} \min_{\mathbf{a} \in \mathcal{T}} \text{COST}(\mathbf{p}_k, \mathbf{a}, \mathbf{u}_m) \ , \tag{3.4}$$

where $\text{COST}(\mathbf{p}_k, \mathbf{a}, \mathbf{u}_m)$ is any cost function that may penalize the triangulated position $\mathbf{p}_k$ given an anchor node position $\mathbf{a}$ and a MPC direction $\mathbf{u}_m$ in the room coordinates system. We point out that a suitable cost function, for a given m, would return a null cost if there exists an anchor $\mathbf{a} \in \mathcal{T}$ that lies exactly on the line leaving $\mathbf{p}_k$ with direction $\mathbf{M}^{(\mathbf{p})}_{:,m}$, otherwise the cost would be greater.

The cost function defined in this thesis is defines as follows

$$\text{COST}(\mathbf{p}_k, \mathbf{a}, \mathbf{u}_m) = \left[\cos^{-1} \left(-\mathbf{u}_m \cdot \frac{\mathbf{a} - \mathbf{p}_k}{\|\mathbf{a} - \mathbf{p}_k\|} \right) \right]^2 w_{\omega(\mathbf{a})} \tag{3.5}$$

where $\mathbf{u}_m = -\mathbf{Q}\mathbf{M}^{(\mathbf{p})}_{:,m}$ and $\omega(\mathbf{a}_n) = \ell$ if $\mathbf{a}_n \in A_\ell$. Note that the function, as it would be desirable, returns a null cost if $-\mathbf{u}_m$ and $\mathbf{a} - \mathbf{p}_k$ are parallel vectors, whereas the cost increases if the minimum angle between any anchor $\mathbf{a} \in \mathcal{T}$ and
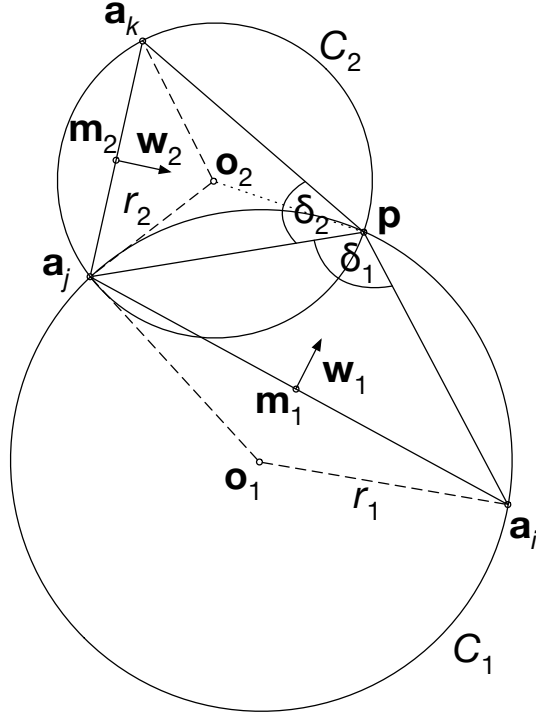
Figure 3.2: The geometry of Angle Difference-of-Arrival localization.

$\mathbf{M}^{(\mathbf{p})}_{:,m}$, with corner in $\mathbf{p}_k$, increases. The square operation penalizes larger discrepancies more than smaller ones (Lines 8 to 14). After computing the argument that returns the minimum cost in (3.4) the anchor $\mathbf{a}$ that minimizes the argument is removed from $\mathcal{T}$ (Line 13). The cost function is exploited in Lines 12 and 13 for these described operations.

The TV steps are repeated for all possible associations of the first two elements of $\mathbf{M}^{(\mathbf{p})}$ to the anchors in the set $\mathcal{A}_\mu$, returning a total of K estimates $\mathbf{p}_k$, $k = 1, \ldots, K$, and their related costs c_k (Line 5). Note that $K \leq |\mathcal{A}_\mu|(|\mathcal{A}_\mu| - 1)$ since the algorithm fails if a triangulated position is found to be outside the room, or if the received AoA spectrum contains fewer than 3 MPCs. The final estimate of $\mathbf{p}$ returned by the TV algorithm is a weighed average of the positions $\mathbf{p}_k$ found along the process (Line 15).

3.3 THE ANGLE DIFFERENCES-OF-ARRIVAL (ADOA) ALGORITHM

The TV algorithm requires the knowledge of the reference angle ϕ_0, or equivalently, of the coordinate transformation matrix $\mathbf{Q}$ introduced in Section 3.2. As this is not necessarily a feasible assumption, and the measurement of ϕ_0 (e. g., as provided by a smartphone's digital compass) may be affected by a significant error, we developed a second algorithm based on the ADoA among MPCs. This algorithm is slightly more complex than TV, but is immune both to errors in ϕ_0 and to variations thereof across the room area.

We start by defining the angles $\delta_1 = \mathbf{M}_{2,2}^{(\mathbf{p})} - \mathbf{M}_{2,1}^{(\mathbf{p})}$ and $\delta_2 = \mathbf{M}_{2,3}^{(\mathbf{p})} - \mathbf{M}_{2,1}^{(\mathbf{p})}$. The ADoA algorithm is described in terms of the following geometrical problem, for which we refer to Figure 3.2: given two points $\mathbf{a}_i$ and $\mathbf{a}_j$ in a 2D space, find the locus of the points $\mathbf{p}$ such that the angle $\widehat{\mathbf{a}_i\mathbf{p}\mathbf{a}_j}$ (where $\mathbf{p}$ is the corner), is constant and equal to the angle δ_1 defined above. This locus is a circumference, of which the segment $\overline{\mathbf{a}_i\mathbf{a}_j}$ is a chord. We assume the angle $\widehat{\mathbf{a}_i\mathbf{p}\mathbf{a}_j}$ to be positive if $\mathbf{a}_i$ follows $\mathbf{a}_j$ in a counterclockwise direction within the space of a semi-circumference and $|\widehat{\mathbf{a}_i\mathbf{p}\mathbf{a}_j}| < \pi$, where the $|\cdot|$ operator in this case represents the absolute value of the angle measure. With reference to Figure 3.2, that depicts a typical ADoA localization scenario, consider the circumference C_1. Given the angle $\widehat{\mathbf{a}_i\mathbf{p}\mathbf{a}_j}$, we have $\widehat{\mathbf{a}_i\mathbf{o}_1\mathbf{a}_j} = 2\,\widehat{\mathbf{a}_i\mathbf{p}\mathbf{a}_j}$, where $\widehat{\mathbf{a}_i\mathbf{o}_1\mathbf{a}_j}$ is the central angle that insists on the same chord $\overline{\mathbf{a}_i\mathbf{a}_j}$. If $\widehat{\mathbf{a}_i\mathbf{p}\mathbf{a}_j} > \pi/2$, $\widehat{\mathbf{a}_i\mathbf{o}_1\mathbf{a}_j}$ is concave, hence $|\widehat{\mathbf{a}_i\mathbf{o}_1\mathbf{a}_j}| > \pi$. In this case, we wrap the angle back into the interval $[-\pi, \pi)$ via the operator $W(\cdot)$. The radius r_1 of C_1 can be found as

$$r_1 = \frac{\|\mathbf{a} - \mathbf{b}\|}{2\sin(|W(\widehat{\mathbf{a}_i\mathbf{o}_1\mathbf{a}_j})|/2)} \ . \tag{3.6}$$

Finally, given $\beta = r_1 \cos\left(W(\widehat{\mathbf{a}_i\mathbf{o}_1\mathbf{a}_j})/2\right)$ and $\mathbf{u} = (\mathbf{a} - \mathbf{b}) \times (0, 0, 1)$, the center of the circumference is found as

$$\mathbf{o}_1 = \mathbf{m}_1 + \text{sgn}\left(W(\widehat{\mathbf{a}_i\mathbf{o}_1\mathbf{a}_j})\right)\frac{\beta\mathbf{u}}{\|\mathbf{u}\|} \ , \tag{3.7}$$

where sgn returns the sign of the angle, and $\mathbf{m}_1 = (\mathbf{a}_i + \mathbf{a}_j)/2$ is the middle point of the chord $\overline{\mathbf{a}_i \mathbf{a}_j}$. The vector

$$\mathbf{w}_1 = \left(\mathbf{o}_1 - \mathbf{m}_1 \right) \operatorname{sgn} \left(W(|\widehat{\mathbf{a}_i \mathbf{o}_1 \mathbf{a}_j}|) \right) \tag{3.8}$$

points to the section of C_1 defined by the chord $\overline{\mathbf{a}_i \mathbf{a}_j}$ where the constant angle requirement is satisfied. We now consider a second chord $\overline{\mathbf{a}_j \mathbf{a}_k}$ and the circumference C_2 as the locus of the points $\mathbf{q}$ where the angle $\widehat{\mathbf{a}_j \mathbf{q} \mathbf{a}_k} = \delta_2$. The radius r_2 and the center $\mathbf{o}_2$ of C_2 can be computed in the same way as above. The point $\mathbf{p}$ of intersection between C_1 and C_2 is considered a feasible location estimate whenever it is located on the sections of C_1 and C_2 pointed to by the orientation vectors $\mathbf{w}_1$ and $\mathbf{w}_2$. This means that, given the two chord centers $\mathbf{m}_1$ and $\mathbf{m}_2$, it must hold that $\mathbf{w}_1 \cdot (\mathbf{p} - \mathbf{m}_1) > 0$ and $\mathbf{w}_2 \cdot (\mathbf{p} - \mathbf{m}_2) > 0$.

The pseudo-code of the procedure that provides an estimate $\hat{\mathbf{p}}$ of the location of a node based on ADoA is given in Algorithm 3. The algorithm starts by determining $\mathcal{A}_\mu$, $\mathbf{M}^{(\mathbf{p})}$, δ_1 and δ_2 (Lines 2 and 3). As for the TV algorithm, we are initially unable to map each detected MPC to its related anchor node. Therefore, the ADoA algorithm collects a set of eligible positions which are the result of the intersection between the circumferences determined by the angle differences δ_1 and δ_2 and the chords $\overline{\mathbf{a}_i \mathbf{a}_j}$ and $\overline{\mathbf{a}_j \mathbf{a}_k}$, $\mathbf{a}_i, \mathbf{a}_j, \mathbf{a}_k \in \mathcal{A}_\mu$. Lines 6 to 8 determine the center and radius of C_1 and C_2 via (3.6) and (3.7), and compute their intersection by checking that it is feasible based on the orientation vectors $\mathbf{w}_1$ and $\mathbf{w}_2$ (see (3.8)). The ADoA procedure is repeated for different triples $(\mathbf{a}_i, \mathbf{a}_j, \mathbf{a}_k) \in \mathcal{A}_\mu$ (Line 5) to yield a number of possible location estimates. Those positions that are valid with respect to the same logical constraints introduced for the TV algorithm are collected in the set $\mathcal{L}$ (Line 9). Because resorting to angle differences does not require to estimate the reference angle ϕ_0, it may happen that for some combinations of anchor nodes, and in the presence of large AoA estimation errors, the user is localized in an erroneous position that still satisfies the angle differences. To eliminate such spurious locations, the estimated position is computed as the median of $\mathcal{L}$ (Line 8).

Algorithm 3: The Angle Difference-of-Arrival algorithm.

1 Function ADoA*($P(\phi)$, $\mathbf{p}_{\text{TX}}$, $\mathcal{Z}$, μ)*

2 $\mathcal{A}_\mu \leftarrow \bigcup_{\ell=0}^{\mu}$ DETERMINEANCHORS$(\ell, \mathbf{p}_{\text{TX}}, \mathcal{Z})$

3   Map $\mathbf{M}^{(\mathbf{p})}$ to canonical base, compute $\boldsymbol{\Delta}$, δ_1, δ_2

4 $\mathcal{L} \leftarrow \varnothing$

5   **foreach** *triple $(\mathbf{a}_i, \mathbf{a}_j, \mathbf{a}_k) \in \mathcal{A}_\mu$, $i \neq j \neq k$* **do**

6 $C_1 \leftarrow$ DETERMINECIRC(i, j, δ_1)

7 $C_2 \leftarrow$ DETERMINECIRC(i, k, δ_2)

8 $\mathbf{p} \leftarrow$ DETERMINEINTERSEC$(C_1, C_2) \setminus \{\mathbf{p}_{\text{TX}}\}$

9   **if** ISVALID$(\mathbf{p}, \mathcal{Z})$ **then** $\mathcal{L} \leftarrow \mathcal{L} \cup \{\mathbf{p}\}$

10   **return** $\hat{\mathbf{p}} \leftarrow$ MEDIAN$(\mathcal{L})$

3.4 LOCALIZATION BASED ON LOCATION FINGERPRINTING (FP)

We finally present a fingerprint-based localization algorithm. We assume that the area the user to be localized within has been previously characterized by creating a database $\mathcal{D}$ of AoA spectra measured at a set of different locations $\mathcal{F} = \{\mathbf{f}_1, \mathbf{f}_2, \ldots\}$ (in Section 2.1.4 this has been called the training phase).

Given a spectrum $P_{\mathbf{p}}(\alpha)$ measured at location $\mathbf{p}$ as an input, the algorithm looks up the most similar spectrum in $\mathcal{D}$ (according to some proximity measure) and returns its corresponding location. In order to be fair to the TV and ADoA schemes, we define the fingerprint of an AoA spectrum in terms of: *i*) a LoS feature, defined as the amplitude and AoA of the LoS arrival; and *ii*) a number of Non-Line of Sight (NLoS) features, defined as the amplitude and ADoA (relative to the LoS AoA) of every other NLoS MPC in the pattern. These choices are based on the fact that the strongest MPC is typically the LoS path [11, 44], and that we wish to make the feature matching process resilient to position-dependent errors in the reference angle ϕ_0. Given the pattern $P_{\mathbf{p}}(\alpha)$ and its MPC matrix $\mathbf{M}^{(\mathbf{p})}$, we identify the LoS feature as a vector $\mathbf{s}^{(\mathbf{p})} = \mathbf{M}^{(\mathbf{p})}_{:,1}$ (it is the strongest MPC since the entries in $\mathbf{M}^{(\mathbf{p})}$ are sorted in decreasing power), and by calling $N_{\mathbf{p}}$ the number of columns in $\mathbf{M}^{(\mathbf{p})}$, we collect the remaining $N_{\mathbf{p}} - 1$ entries of $\mathbf{M}^{(\mathbf{p})}$ in the NLoS feature matrix $\mathbf{T}^{(\mathbf{p})}$ and subtract the angle of the LoS path

$\mathbf{M}_{2,1}^{(\mathbf{p})}$ from all elements of $\mathbf{T}_{2,:}^{(\mathbf{p})}$. In the pseudo-code reported in Algorithm 4, this corresponds to Line 2.

Note that the AoA spectra received at any two different points typically have one LoS feature, and may have a different number of NLoS features. For each entry of $\mathcal{D}$ measured at location $\mathbf{f}$ (Line 3), we execute an adapted instance of the closest point algorithm [51] which returns the indices i and j of the NLoS features in $\mathbf{T}^{(\mathbf{p})}$ and $\mathbf{T}^{(\mathbf{f})}$, respectively, whose angle differences are most similar. The pseudo-code for the algorithm is reported in Algorithm 5: the function GETCLOSESTPAIRS($\mathbf{X}$, $\mathbf{Y}$) takes as input two real-valued vectors $\mathbf{X}$ and $\mathbf{Y}$ of possibly different length and returns a set $\mathcal{P}$ of couples of the indexes of the closest values from the two vectors; GETCLOSESTPAIRS($\mathbf{X}$, $\mathbf{Y}$) makes use of NEAREST($\mathbf{X}$,y) which given a vector $\mathbf{X}$ returns the index of the closest value to the given input y.

Now that we can pair MPCs from different AoA spectra, we need a cost function to characterize the similarity of the patterns at $\mathbf{p}$ and $\mathbf{f}$.

We design the cost function as follows:

$$
\begin{aligned}
c_{\mathbf{f}} = {} & -w_{\ell a}\left|\mathbf{s}_{2,1}^{(\mathbf{p})} - \mathbf{s}_{2,1}^{(\mathbf{f})}\right| - 2w_p \frac{|\mathbf{s}_{1,1}^{(\mathbf{p})} - \mathbf{s}_{1,1}^{(\mathbf{f})}|}{\mathbf{s}_{1,1}^{(\mathbf{p})} + \mathbf{s}_{1,1}^{(\mathbf{f})}} \\
& - \sum_{\forall (i,j) \in \mathcal{P}} \left(w_{na}\left|\mathbf{T}_{2,i}^{(\mathbf{p})} - \mathbf{T}_{2,j}^{(\mathbf{f})}\right| + 2w_p \frac{|\mathbf{T}_{1,i}^{(\mathbf{p})} - \mathbf{T}_{1,j}^{(\mathbf{f})}|}{\mathbf{T}_{1,i}^{(\mathbf{p})} + \mathbf{T}_{1,j}^{(\mathbf{f})}} \right) \; ,
\end{aligned}
\tag{3.9}
$$

where the weights $w_{\ell a}$, w_{na} and w_p are chosen to give more importance to the discrepancies in the angle differences of NLoS paths rather than to the absolute difference among the angles of the LoS path: this makes fingerprinting-based localization more robust to possible errors in the reference angle ϕ_0. On the contrary, the amplitude discrepancies of the paired LoS and NLoS features is given the same weight w_p. The cost function can be seen as the logarithm of a product of exponential functions where the arguments are a function of the differences between angle and amplitude values of the MPCs of the pattern in $\mathbf{f}$ and $\mathbf{p}$, and the weights $w_{\ell a}$, w_{na} and w_p may be seen as variances. We compute the absolute value of the angle differences since we have verified empirically that it achieves better robustness compared to, e. g., the squared value of the difference.

In Algorithm 4, the function LOSCOST in Line 4 of computes the first line in (3.9), whereas the function MPCCOST repeatedly called in Lines 6 and 7 computes the sum in (3.9). Finally, the algorithm returns the estimated position $\hat{\mathbf{p}}$ as the the location of the entry $\mathbf{f}$ in $\mathcal{F}$ that has minimum cost (Line 8).

Algorithm 4: Localization based on location fingerprints.

1 Function FINGERPRINT$(P_{\mathbf{p}}(\alpha),\ \mathcal{D})$
2 $\quad$ Compute $\mathbf{M}^{(\mathbf{p})}$, extract $\mathbf{s}^{(\mathbf{p})}$ and $\mathbf{T}^{(\mathbf{p})}$
3 $\quad$ **foreach** $P_{\mathbf{f}}(\alpha) \in \mathcal{D}$ **do**
4 $\qquad$ $c_{\mathbf{f}} \leftarrow$ LOSCOST$(\mathbf{s}^{(\mathbf{p})}, \mathbf{s}^{(\mathbf{f})})$
5 $\qquad$ $\mathcal{P} \leftarrow$ CLOSESTPAIRS$\left(\mathbf{T}^{(\mathbf{p})}_{2,:}, \mathbf{T}^{(\mathbf{f})}_{2,:}\right)$
6 $\qquad$ **foreach** *pair* $(i,j) \in \mathcal{P}$ **do**
7 $\qquad\quad$ $c_{\mathbf{f}} \leftarrow c_{\mathbf{f}} +$ MPCCOST$\left(\mathbf{T}^{(\mathbf{p})}_{:,i}, \mathbf{T}^{(\mathbf{f})}_{:,j}\right)$
8 $\quad$ **return** $\hat{\mathbf{p}} \leftarrow \arg\min_{\mathbf{f}} c_{\mathbf{f}}$

Algorithm 5: The closest pairs algorithm used to detect closest pairs of real numbers taken from two lists.

1 Function GETCLOSESTPAIRS$(\mathbf{X},\ \mathbf{Y})$
2 $\quad$ $\mathcal{P} \leftarrow \varnothing$
3 $\quad$ **for** $j = 1$ **To** $n\_elem(\mathbf{X})$ **do**
4 $\qquad$ $b \leftarrow$ NEAREST$(\mathbf{Y}, \mathbf{X}(j))$
5 $\qquad$ **if** $j =$ NEAREST$(\mathbf{X}, \mathbf{Y}(b)$ **then**
6 $\qquad\quad$ $\mathcal{P} \leftarrow \mathcal{P} \cup \{(j,b)\}$
7 $\quad$ **return** $\mathcal{P}$

8 Function NEAREST$(\mathbf{X}, y)$
9 $\quad$ $d_{\min} \leftarrow \infty$
10 $\quad$ **for** $k = 1$ **To** $n\_elem(\mathbf{X})$ **do**
11 $\qquad$ **if** $|\mathbf{X}(k) - y| < d_{\min}$ **then**
12 $\qquad\quad$ $min \leftarrow |\mathbf{X}(k) - y|$
13 $\qquad\quad$ $el \leftarrow k$
14 $\quad$ **return** el

PERFORMANCE EVALUATION BY SIMULATION

4.1 A RAY TRACING TOOL

In order to evaluate the performance of the localization algorithms in controlled ideal and non-ideal conditions, we have developed a ray tracer, which is an appropriate tool to model the propagation of MMW in an indoor environment given the directionality of MMW transmissions [11, 44] and the limited amount of scattering generated by reflections [43].

The ray tracer simulates the propagation of a MMW ray given the location of the transmitter, its transmission beam pattern, the boundaries of the propagation area, the location of the receiver and its reception beam pattern.

In the following, we consider the simulation of a single ray departing from the transmitter position $\mathbf{p}_{\mathrm{TX}}$. Denote as $\{\mathbf{x}_n\}_{n=0,1,2,\dots}$ the sequence of positions through which the ray propagates. Given a ray departing from the transmitter at a given position $\mathbf{p}_{\mathrm{TX}}$, we have $\mathbf{x}_0 = \mathbf{p}_{\mathrm{TX}}$. Denote as $\{\mathbf{u}_n\}_{n=0,1,2,\dots}$ the sequence of the unit-norm propagation direction vectors of the ray at the corresponding positions $\mathbf{x}_n$. Given the initial ray propagation direction $\mathbf{u}_0$, the ray propagation is modeled by updating the position of the ray $\mathbf{x}_n$ as

$$\mathbf{x}_{n+1} = \mathbf{x}_n + \Delta x \mathbf{u_n}, \tag{4.1}$$

where Δx is a constant which regulates the accuracy of the simulation.

After every update of the position, the simulator has to check if some logical constraints are violated. For example we may check if the position $\mathbf{x}_i$ lays outside the room boundaries: given a surface S with a normal vector $\mathbf{n}$ of an object $\mathbf{o} \in \mathcal{Z}$, and a point $\mathbf{q} \in S$, if $(\mathbf{x}_n - \mathbf{q}) \cdot \mathbf{n} > 0$ then $\mathbf{x}_n$ still has not impacted on the surface. If no violated constraints are detected, the ray direction is not updated, i.e. $\mathbf{u}_{i+1} = \mathbf{u}_n$; otherwise a reflection must be modeled, and this translates to a
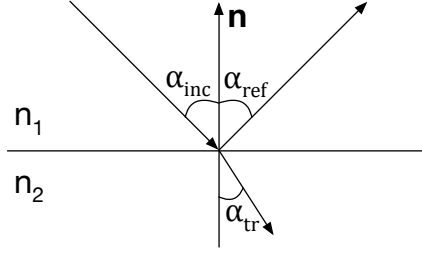
Figure 4.1: Refraction and reflection of a wave at the interface between two media of different refractive indices n_1 and n_2.

variation in the direction vector. We modeled the bounces using Snell's law as per [43]: given a ray with direction $\mathbf{u}_n$, reflecting off a surface S with normal vector $\mathbf{n}$, the direction $\mathbf{u}_{n+1}$ of the reflected ray is computed as

$$\mathbf{u}_{i+1} = \mathbf{u}_n - 2(\mathbf{u}_n \cdot \mathbf{n})\mathbf{n}. \tag{4.2}$$

Along with the trajectory modeling, the signal power must be taken into account. First, we consider that the ray incurs standard distance-dependent path loss $P_L(d)$ [52] as it was introduced in: Section 2.1.1

$$P_L(d) = P_{LFS}(d_0) + 10\gamma \log_{10}\left(\frac{d}{d_0}\right), \tag{4.3}$$

where d is the distance covered by the signal, P_{LFS} the free space path loss at a reference distance d_0 and γ is the path loss exponent (set to $\gamma = 2$ [44] in our simulations). Notice that the distance d covered by the ray can be parametrized as $n\Delta x$, $n = 0, 1, 2, \ldots$ and thus the path loss can be updated as

$$P_L(\Delta x(n+1)) = P_L(\Delta xi) + 10\gamma \frac{d_0}{n\Delta x \ln(10)} \tag{4.4}$$

If the obstacles are not perfect reflectors, a power loss must also be taken into account. A simple model would be to consider a constant power loss at each bounce, determined by the kind of surface where the reflection took place (e.g. it may be a function of the refraction index of the material). A more exhaustive model would express the power loss as a function of the angle of incidence α_{inc}:

in this case, Fresnel's equations shall be exploited. Referring to Figure 4.1, when a wave encounters an interface between a medium with a refraction index n_1 and a medium with refraction index n_2, it splits into two waves lying on the plane which contains the incidence plane, and that is orthogonal to the normal vector $\mathbf{n}$ describing the interface: the reflected wave travels back in the first medium with an angle α_{ref}, whereas the refracted wave propagates in the second medium with an angle α_{tr}. Snell's equations establish that $\alpha_{\text{ref}} = \alpha_{\text{inc}}$ and $n_1 \alpha_{\text{inc}} = n_2 \alpha_{\text{tr}}$. If the incident wave is polarized with its electric field perpendicular to the plane containing the incident, reflected, and refracted rays we refer the wave as s-polarized. Instead, if the incident wave is polarized with its electric field parallel to the plane of incidence we refer the wave as p-polarized. Defining the reflection (and refraction) indexes r_s and r_p (t_s and t_p) as the ratio between the reflected (refracted) wave amplitude and the incident wave amplitude s-polarized and p-polarized respectively, Fresnel's equations states that

$$r_s = \frac{n_1 \cos \alpha_{\text{inc}} - n_2 \cos \alpha_{\text{tr}}}{n_1 \cos \alpha_{\text{inc}} + n_2 \cos \alpha_{\text{tr}}} \qquad r_p = \frac{n_1 \cos \alpha_{\text{tr}} - n_2 \cos \alpha_{\text{inc}}}{n_1 \cos \alpha_{\text{tr}} + n_2 \cos \alpha_{\text{inc}}}. \qquad (4.5)$$

Defining the reflectance as the fraction of the incident electromagnetic power that is reflected at an interface, Equation(4.5) leads to the following equations for the reflectance R_s and R_p for s-polarization and p-polarization respectively

$$R_s = \left| \frac{n_1 \cos \alpha_{\text{inc}} - n_2 \cos \alpha_{\text{tr}}}{n_1 \cos \alpha_{\text{inc}} + n_2 \cos \alpha_{\text{tr}}} \right|^2 \qquad R_p = \left| \frac{n_1 \cos \alpha_{\text{tr}} - n_2 \cos \alpha_{\text{inc}}}{n_1 \cos \alpha_{\text{tr}} + n_2 \cos \alpha_{\text{inc}}} \right|^2. \qquad (4.6)$$

It the wave is not polarized the reflectance is $R = (R_s + R_p)/2$. To summarize, if a wave propagating in a medium with a given refraction index n_1 bounces off an obstacle with refraction index n_2, with incidence angle αi, a power loss of $10 \log_{10} R(\alpha_{\text{inc}}, n_1, n_2)$ [dB] (if the wave is assumed to be non-polarized) has to be added to the ray's path loss in Equation 4.4.

Algorithm 6 is the pseudo-code used for tracing a ray departing from the transmitter position $\mathbf{p}_{\text{TX}}$ with direction $\mathbf{u}_0$ and initial power p_0. The simulation of the ray propagation continues until a certain threshold value p_{lim} of the signal power

---

Algorithm 6: Localization based on location fingerprints.

1 Function TRACERAY$(\mathbf{x}_0, \mathbf{u}_0, p_0, \mathcal{Z}, \epsilon, \Delta x, p_{\text{lim}})$
2 $p \leftarrow p_0$, $\mathbf{x} \leftarrow \mathbf{x_0}$, $r \leftarrow 0$, $d \leftarrow 0$
3   **while** $p > p_{\text{lim}}$ **do**
4 $\mathbf{x} \leftarrow \mathbf{x} + \Delta x \mathbf{u}$
5 $d \leftarrow d + \Delta x$ **foreach** $\mathbf{o} \in \mathcal{Z}$ **do**
6   **foreach** *surface S of* $\mathbf{o}$ **do**
7   **if** *given* $\mathbf{q} \in S$, $(\mathbf{x} - \mathbf{q}) \cdot \mathbf{n} < 0$ **then**
8   Ray has hit an obstacle!
9 $r \leftarrow r + 1$
10 $p \leftarrow p - \text{POWERLOSS}(\mathbf{u}, \mathbf{n})$
11 $\mathbf{u} \leftarrow \mathbf{u} - 2(\mathbf{u} \cdot \mathbf{n})\mathbf{n}$
12   **Break**

13   **if** *No obstacle has been hit* **then**
14 $p \leftarrow p - \text{PATHLOSS}(\Delta x)$
15   **if** $\|\mathbf{x} - \mathbf{p}_{\text{RX}}\| < \epsilon$ **then**
16   Save the eigenray parameters, e. g. p, $\mathbf{u}$, $\mathbf{u}_0$, r

---

is reached. Notice that the signal simulation does not end if the ray travels near the receiver position $\mathbf{p}_{\text{RX}}$. The function POWERLOSS$(\mathbf{u}, \mathbf{n})$ in Line 10 computers the power loss due to a reflection: a constant power loss can be assumed, otherwise it may be a function of the incidence angle α_{inc} derived by ray direction vector $\mathbf{u}$ and the surface normal vector $\mathbf{n}$ where the reflection took place; otherwise, the power loss may be computed according to reflectance calculated as in Equation (4.6). The function PATHLOSS(Δx) in Line 14 computes the differential path loss that results from a propagation of Δx: Line 14 implements as Equation 4.4.

Given the transmission beam pattern of the transmitter's antenna, expressed as $P_{\text{TX}}(\phi, \theta)$ where $\phi \in [0, 2\pi)$ is the azimuthal angle and $\theta \in [-\pi/2, \pi/2]$ the elevation angle, a complete simulation shall be obtained by executing instances of the ray tracer that spans the ranges of values for ϕ and θ: the initial power p_0 is set as $P_{\text{TX}}(\phi, \theta)$ (this models the directivity of the antenna) and the initial direction vector is $\mathbf{u}_0 = (\cos\phi\sin\theta, \sin\phi\sin\theta, \cos\theta)$. The rays that lead to an actual received power contribution at the receiver (or eigenrays) are identified as those that propagate sufficiently close to the receiver, i. e. rays such that

$\exists i : \|\mathbf{x}_i - \mathbf{p}_{\text{RX}}\| < \epsilon$ (ϵ is a parameter of the ray tracer and should be inversely proportional to the number of rays that are going to be simulated). These rays are stored in a list of eigenrays (Line 16) which constitutes the output of the whole simulation.

Considering eigenrays in the azimuthal plane ($\phi = 0$), an impulsive version of the AoA spectrum $P^*_{\mathbf{p}_{\text{RX}}}(\phi)$ can be obtained. If the reception beam pattern $P_{\text{RX}}(\phi, \theta)$ of the receiver antenna is known, the effective AoA spectrum $P_{\mathbf{p}_{\text{RX}}}(\phi)$ can be obtained correlating $P^*_{\mathbf{p}_{\text{RX}}}(\phi)$ with $P_{\text{RX}}(\phi, 0)$: for directive antennas, this models the fact that possible side lobes in the reception pattern give a power contribution as well. For instance, if an isotropic antenna is deployed as the receiving antenna, then $P^*_{\mathbf{p}_{\text{RX}}}(\phi)$ assumes a constant value. Obviously, the obtained AoA spectrum can be exploited as an input for the three localization algorithms devised. The following Section 4.2 will employ simulated AoA spectra in order to evaluate the performance of the three algorithms.

Finally, notice that the ray tracer can also be exploited to obtain the PDP at the receiver position $\mathbf{p}_{\text{RX}}$: in fact, each eigenray that has covered a distance d to reach the receiver gives a power contribution at a time $t = d/v$, where v is the propagation speed of the wave ($v \simeq c$ if the medium is the air). As it will be clearer later, our algorithms mainly rely on AoA, therefore we will not use PDP information, and leave extensions of the algorithms that make use of it as a future work.

4.2 SIMULATION SCENARIO AND RESULTS

Our simulation scenario consists of a rectangular empty room of size $8.9 \times 6.3 \times 3$ m. The reference of the Cartesian coordinate system is placed at the south-western corner of the room, where the x axis extends towards East and the y axis towards North. The walls, floor and ceiling are modeled as uniform flat surfaces with a constant refraction index n_2. We set $\phi_0 = \pi/2$, i.e., angles are measured in a counterclockwise direction starting from the south-to-north direction. The transmitter is located at $\mathbf{p}_{\text{TX}} = (0.2, 0.2, 1)$m. We assume the transmitter employs a

omnidirectional antenna, i.e., $P_{\mathrm{TX}}(\phi, \theta)$ is constant for every value of ϕ and θ. Instead, the receiver antenna is modeled as a perfect directional antenna with a reception beam pattern that can be modeled as $P_{\mathrm{RX}}(\phi, 0) = \delta(\phi)$ ($\delta(x)$ is the Dirac delta function, i.e. $\delta(x)$ equals 1 if $x = 0$, 0 otherwise).

We characterize the performance of the three algorithms via two quantities:

- the empirical Cumulative Density Function (CDF) of the Localization Error (LE), i.e. the function that returns the fraction of estimates with an error lower than a given value;

- the localization failure probability P_u, i.e. the probability that the localization algorithm fails to estimate a position.

For all algorithms, we truncate the set of virtual anchors positions $\mathcal{A}$ to $\mathcal{A}_2$, i.e. considering only the virtual anchor nodes up to the second order ($\mu = 2$). This choice derives from [44] where the authors claim that reflections up to the second order give a power contribution.

The fingerprinting database $\mathcal{D}$ is populated with simulated AoA spectra retrieved at the points in the training set $\mathcal{F}_1 = \{(1.85 + 1.3k,\ 1.85 + 1.3n,\ 1),\ k = 0, \ldots, 4,\ n = 0, 1, 2\}$: these constitute a grid of 15 points equally spaced $1.3\,\mathrm{m}$ apart from their nearest neighbors, and centered inside the room. The height of the measurement points in $\mathcal{F}_1$ is the same as that of the transmitter, i.e. $1\,\mathrm{m}$.

We have also simulated the fact that the measurement of the AoA spectrum by the node to be localized is not ideal, but rather may be affected by errors on the reference angle ϕ_0 (for example due to a wrong calibration of the compass) and by errors on the absolute estimates of the AoA of the MPCs (for example, as a consequence of small changes in the propagation environment, or due to imperfect beamforming of the phased antenna array at the receiver). This non-ideal behavior has been simulated according to the Gaussian Angle of Arrival (GAA) model [53] which assumes the AoA of a multipath component coming from a single scatterer cluster, e.g. a wall, to be Gaussian-distributed around the direction predicted by Snell's law for reflections. Thus, errors on the absolute estimates of the AoA of the MPCs, for a given position $\mathbf{p}$, are simulated by first estimating the true AoA
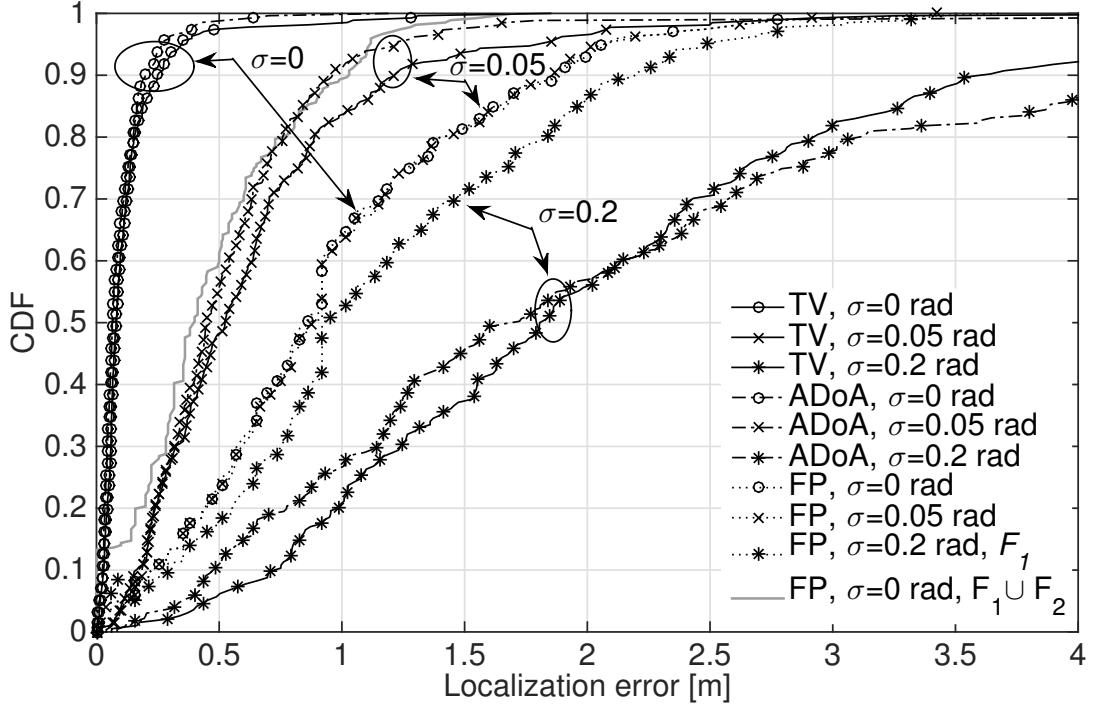
Figure 4.2: Localization error CDF for all algorithms for different values of the MPC AoA estimation error σ.

spectrum, by extracting the MPC matrix $\mathbf{M^{(p)}}$ and by adding a different random Gaussian-distributed displacement of standard deviation σ to each element of $\mathbf{M}_{2,:}^{(\mathbf{p})}$.

The CDF for the LE is graphically reported in Figure 4.2 for the ideal case where $\sigma = 0\,\mathrm{rad} = 0°$ and the non-ideal cases for $\sigma = 0.05\,\mathrm{rad} = 2.86°$ and for $\sigma = 0.2\,\mathrm{rad} = 11.45°$.

In the ideal case where $\sigma = 0°$, both the TV and the ADoA algorithms localize nodes with sub-meter accuracy, where the 90th percentile of the LE is about $0.25\,\mathrm{m}$. In this respect, they consistently outperform FP, which experiences a double maximum LE and sub-meter accuracy up to the 65th percentile.

For increasing values of σ, the performance of all algorithms degrades. For $\sigma = 2.86°$, $\approx 90\,\%$ of TV's and ADoA's estimates achieve sub-meter accuracy. For considerably larger AoA estimation errors, corresponding to $\sigma = 11.45°$, location estimates become expectedly less accurate, with a median error of $\approx 1.7\,\mathrm{m}$ for both ADoA and TV. Setting $\sigma = 0.1\,\mathrm{rad} = 5.73°$ would translate into a

Table 4.1: The localization failure probability, and the probability of achieving a LE below 1 m, and for the three algorithms under different values of σ.

	P_u			$\mathbb{P}[\text{LE} \leq 1\,\text{m}]$		
	TV	ADoA	FP	TV	ADoA	FP
$\sigma = 0°$	0	0	0	0.984	0.998	0
$\sigma = 2.86°$	0.018	0.029	0	0.836	0.912	0
$\sigma = 5.73°$	0.107	0.070	0	0.479	0.564	0
$\sigma = 11.45°$	0.284	0.147	0	0.208	0.267	0

median LE around 1 m, and has been omitted for clarity in Figure 4.2. For the TV algorithm, the error increases both because the triangulation step relies on sufficiently accurate AoA information, and because the estimated AoAs of the MPCs do not exactly correspond to the virtual anchors in $\mathcal{A}_\mu$. For the ADoA algorithm, instead, angle differences are affected by errors of variance $2\sigma^2$, and negatively affect the estimation of the intersection between the circumferences in Figure 3.2.

Thanks to the matching operation carried out by the closest pair algorithm (see Algorithm 4), FP is more robust to high values of σ, and its performance does not degrade significantly even for $\sigma = 0.2$. The LE incurred by TV and ADoA is lower than that of fingerprinting for $\sigma = 0°$ and $\sigma = 2.86°$, and becomes worse for $\sigma = 11.45°$.

Notice that one of the factors that affects the LE of the FP algorithm is the cardinality of the training set $\mathcal{D}$: for example, if all the training set points are spaced by Δx, assuming that localization maps to the nearest point, the LE may be up to $\Delta x/2$. Thus, the LE of the fingerprinting algorithm can be improved by increasing the cardinality of the training set. Related to our simulation, call $\mathcal{F}_2 = \{(1.2 + 1.3k, 1.2 + 1.3n, 1), k = 0, \ldots, 6, n = 0, \ldots, 3\}$. By populating $\mathcal{D}$ with the patterns measured at the points of $\mathcal{F}_1 \cup \mathcal{F}_2$, the error of the FP algorithm improves to match that of TV and ADoA for $\sigma = 2.86°$.

The performance in terms of localization failure probability is reported in Table 4.1. In the same table we have also reported the probability that the LE is

below $1\,\mathrm{m}$, a quantity defined as $\mathbb{P}[\mathrm{LE} \leq 1\,\mathrm{m}]$. Since, the matching operation in the FP algorithm always permits to localize, it results that $P_u = 0$ for FP. For TV and ADoA algorithms, as expected, the localization failure probability increases for larger values of σ: besides the ideal case in which both the algorithms never fail, the ADoA algorithm results to be more robust than the TV algorithm, with a lower value for P_u for the same σ.

Finally, we have devised another simulation which may model the fact that the user to be localized has an equipment that only provides a discretized version of the AoA spectrum. For example, this may be the case where the receiver is made up by a limited number of directional antennas. Thus, we aim to evaluate the robustness, in terms of LE, and localization failure probability as well, of the three algorithms if a granularity in the AoA spectrum is present.

To this purpose, Figure 4.3 presents the performance of the TV and ADoA algorithms when the AoA spectra are sampled with a limited precision $\Delta\phi$, for $\sigma = 0°$. The results show that increasing $\Delta\phi$ causes the increase both of the average LE and of the probability P_u of being unable to localize a node. Both the TV and the ADoA algorithms are similarly affected by the increase of $\Delta\phi$. Interestingly, we observe that the average LEs remain lower than $1\,\mathrm{m}$, with $P_u < 0.05$ for $\Delta\phi \leq 10°$.
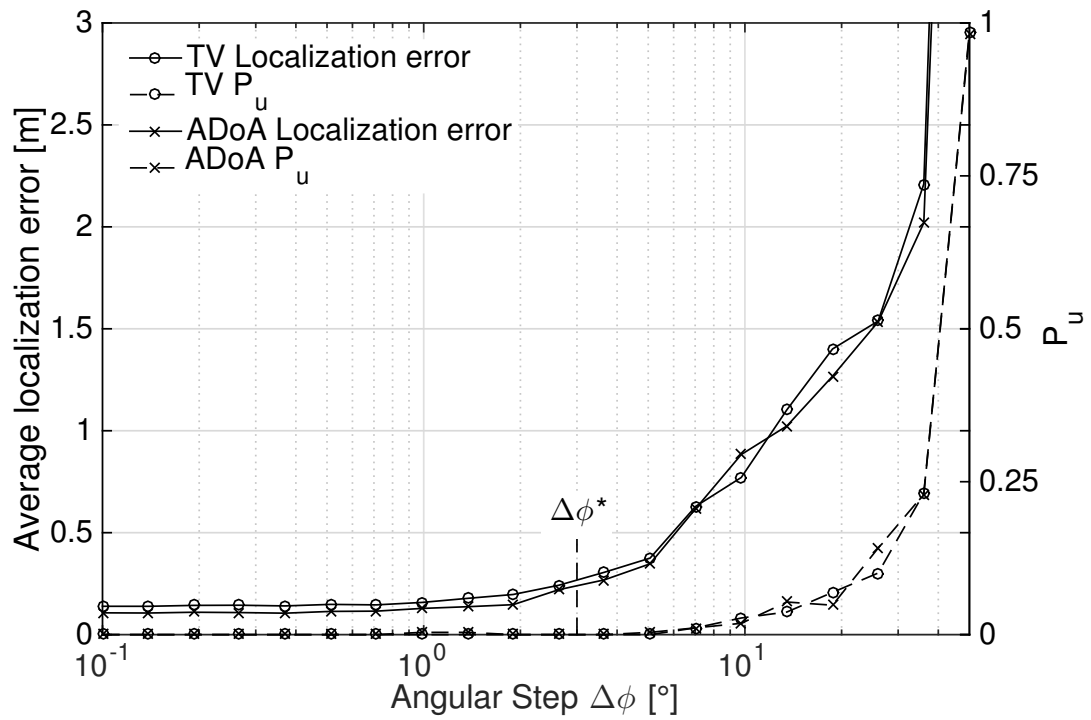
Figure 4.3: Localization error and probability of localization failure P_u for the TV and the ADoA algorithms as a function of the angular step $\Delta\phi$. The granularity chosen for the measurements in Section 5.1 is marked as $\Delta\phi^*$.

5

EXPERIMENTAL RESULTS

In this chapter we present our experimental evaluation of the localization algorithms. Section 5.1 describes the measurement equipment and the methodology that we devised to obtain experimental AoA spectra. In Section 5.2 we report the performance evaluation of the three algorithms when experimental AoA spectra are employed, and discuss the results with those obtained in Section 4.2.

5.1 EQUIPMENT AND EXPERIMENTAL METHODOLOGY

In order to evaluate the performance of our localization algorithms in the presence of actual MMW transceivers, we devised a campaign of measurements in an empty room available at the ground floor of the IMDEA Networks Institute premises[1]: the room is numbered 1.23 and it is sized $8.9 \times 6.3 \times 3$ m for a total of $56.26 \, \text{m}^2$. We note that the room size is the same as the one we set for the simulations in Section 4.2. A plan of the room is reported in Figure 5.1. The reference system is also set as in Section 4.2, where the origin of the Cartesian coordinate system is placed at the south-western corner of the room, the x axis extends towards east and the y axis towards north. Between all the available rooms, we selected this one in order to guarantee that the LoS MMW signal and its reflections could be

1 The measurement campaign has been carried out in collaboration with the IMDEA Wireless Networking group, coordinated by Prof. Joerg Widmer.
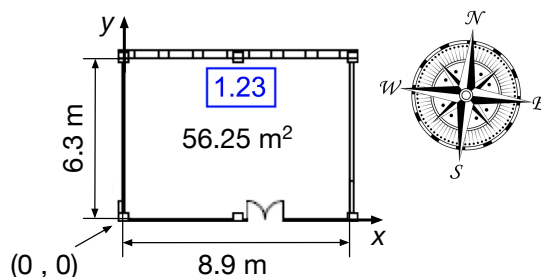

Figure 5.1: Plan of the the room selected for the campaign of measurements.

comfortably heard at all locations in the room. In larger rooms, the signal of the AP would be excessively attenuated, impeding single-AP localization: a solution may be to exploit a more powerful AP; another solution may be a multiple AP deployment, since all the three algorithms can be straightforwardly extended to the latter case.

As a MMW transmitter we employed the Dell D5000 wireless docking station (see Figure 5.2):[2] it is one of the first available off-the-shelf hardware that exploits MMW frequencies and whose specifications are standardized by the Wireless Gigabit Alliance (WiGig), a trade association that promotes the adoption of wireless technologies exploiting the 60 GHz frequency band. As for the simulations in Section 4.2, the transmitter was placed at the position $\mathbf{p}_{TX} = (0.2, 0.2, 1)$m, i.e. close to the south-western room corner. As a receiver, we employed the 60 GHz Vubiq development system[3] equipped with a 25 dBi standard gain horn antenna mounted on an Arduino-controlled rotating stage. An Agilent MSO-X 3034 oscilloscope is finally connected to the Vubiq board in order to collect the received signals and store them in a computer for further processing.

In order to obtain the AoA spectra useful to test the algorithms, we exploited the D5000 device discovery process. As explained in Section 2.3.2, MMW communications rely on directive antennas in order to face the high power loss exhibited at these frequencies: clearly, if the transmitter and the receiver main lobes are not pointing toward each other, the communication will be very likely compromised, and this is the motivation behind the preliminary phase of the device discovery. In the case of the D5000 docking station, the device discovery is a process defined by the 60-GHz WiGig protocol: this involves the transmission of 32 discovery frames, each corresponding to a different configuration of the station's 2×8 phased antenna array. An example of signal received during this process is shown in Figure 5.4. These device discovery frames are sent periodically every 102.4 ms.

---

2 http://i.dell.com/sites/doccontent/shared-content/data-sheets/en/Documents/ Dell-Wireless-Dock-WiGig-spec-sheet.pdf

3 http://www.admiral-microwaves.co.uk/pdf/vubiq/V60WGD02.pdf

Figure 5.2: The Dell D5000 wireless docking station employed as a transmitter.

Figure 5.3: The Vubiq development system, equipped with a 60 GHz horn antenna, employed as a receiver.
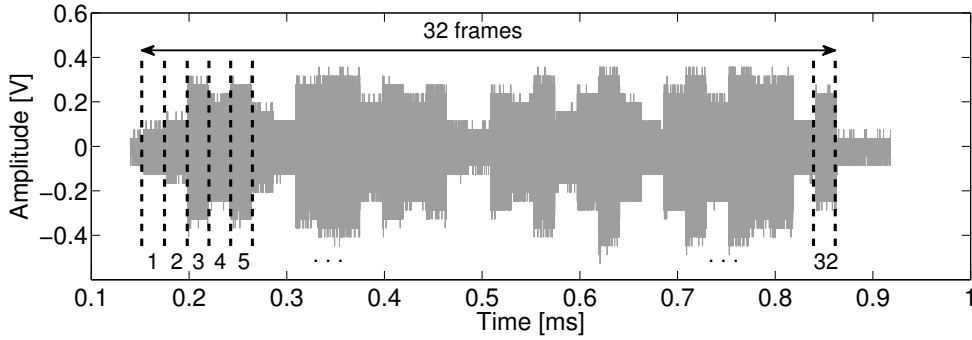

Figure 5.4: Dell D5000's device discovery frames. Each frame corresponds to a different configuration of the station's 2×8 phased antenna array.

The Vubiq system is employed to reveal LoS receptions as well as any MultiPath Component (MPC) reflected off the boundaries of the room at any given position. This is done by redirecting the Vubiq's down-converted, 1.8 GHz-bandwidth, modulated signal traces of the analog I/Q output directly into the oscilloscope, which stores traces for later analysis. The process makes it possible to collect the voltage amplitude of each of the 32 discovery frames over the azimuthal plane, for a number of orientations spaced by $\Delta\phi^* = 3°$. This value has been chosen in order to achieve a reasonable tradeoff between measurement time and accuracy, and because Figure 4.3 suggests that neither the localization error nor P_u would be significantly affected. For every orientation, the receiver always captures the
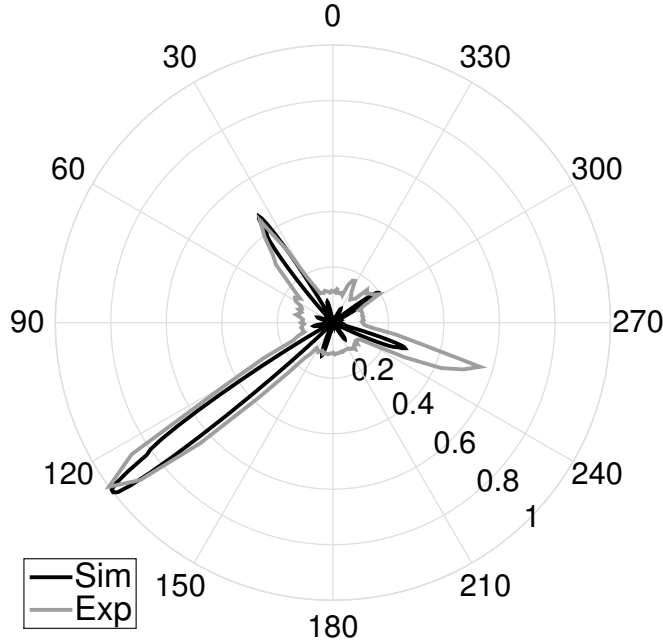
Figure 5.5: The simulated and experimental AoA spectrum at the position $(5.75, 4.45, 1)$m.

same number of frames as in Figure 5.4, with different voltage amplitudes that depend on the antenna patterns used by the D5000 for each frame, and on how the MMW signal is reflected off the boundaries and obstacles of the room.

From these traces, the value of the AoA spectrum $P(\phi)$ for a given angle ϕ multiple of $\Delta\phi$ is extracted by measuring the voltage amplitude of the strongest frame. This yields robustness against the presence of small sidelobes in the transmitter's pattern. Since parameters such as the impedance of the oscilloscope's probe were unknown, and thus it would be impossible to determine the power from the voltage amplitude measure, the obtained AoA spectra have been normalized, i. e. the range of values is $[0, 1]$. In this case, it is easy to pass from voltage to power or vice-versa with a square or square root operation, respectively. An immediate consequence of normalization is that the FP algorithm may be stressed since it relies on amplitude information as well, unlike TV and ADoA.

Figure 5.5 shows one of the experimental normalized patterns (in gray), measured at position $(5.75, 4.45, 1)$m (the point marked by a diamond in Figure 5.6). We observe that the LoS path between the D5000 and the Vubiq has an AoA
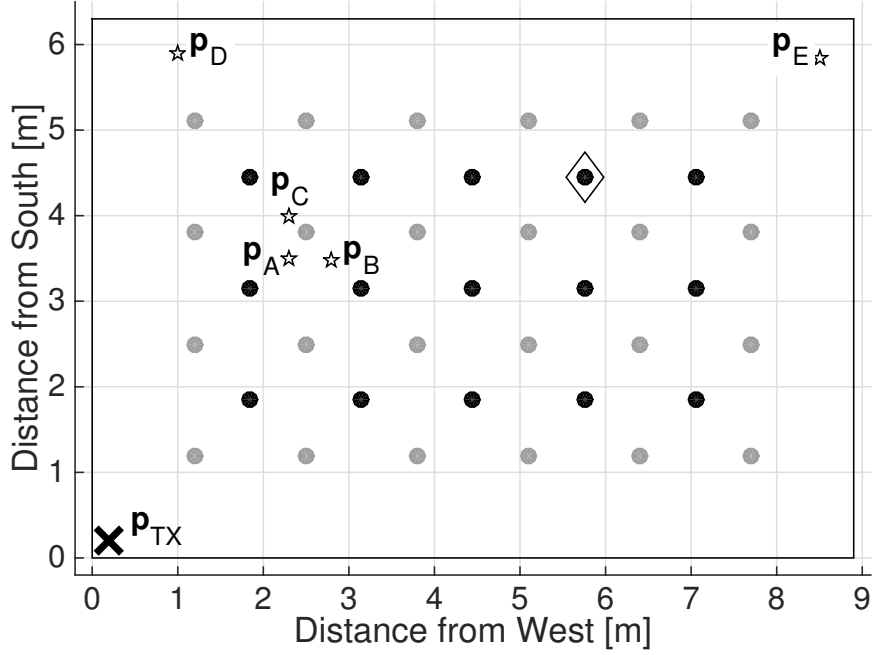
Figure 5.6: Experimental measurement grid. Black: $\mathcal{F}_1$; gray: $\mathcal{F}_2$; diamond: measurement point for the AoA spectrum shown in Figure 5.5.

of 125°; strong reflections are detected with AoAs of 35° and 250°, and a weaker reflection has an AoA of 300°. For comparison, we also plot the normalized AoA spectrum simulated via ray tracing at the same position (in black), which proves the very good agreement between simulations and measurements. The reception beam pattern of the receiver antenna has been modeled as $P_{\mathrm{RX}}(\phi, 0) = \exp\left(-\frac{\phi^2}{2s^2}\right)$, $s = 0.1$. The gaussian shape and the value of the parameter s have been devised empirically.

Figure 5.7 on page 55 visualizes the pattern in Figure 5.5 placed inside the room at the measurement position $(5.75, 4.45, 1)$m (for visualization purposes we have not considered all the possible VAs). As can be seen, both the simulated and the experimental AoA spectra are perfectly in agreement with with the MPCs that would be expected at that position: the NLoS MPCs directions are in accordance with the position of the VA, of first order (VAs at position $\mathbf{a}_i$ and $\mathbf{a}_j$ both belonging to A_1) and second order (VA at position $\mathbf{a}_k \in A_2$). Figures 5.5 and 5.7 further confirm that the devised algorithms are suitable for experimental data too.

In order to collect a feasible amount of AoA spectra for performance evaluation, in a reasonable amount of time, we carried out AoA spectrum measurements at the 39 grid points shown in Figure 5.6. In the figure, the black and gray points respectively correspond to the sets $\mathcal{F}_1 = \{(1.85 + 1.3k,\ 1.85 + 1.3n,\ 1),\ k = 0, \ldots, 4,\ n = 0, 1, 2\}$ and $\mathcal{F}_2 = \{(1.2 + 1.3k,\ 1.2 + 1.3n,\ 1), k = 0, \ldots, 6,\ n = 0, \ldots, 3\}$ discussed in Section 4.2: the two grids span the room uniformly and would give a fair performance evaluation since we expect a position-dependent LE of the algorithms. Moreover, the presence of 2 grids will be useful to build a training set for the FP algorithm as will be explained in Section 5.2. In addition to the grid points, we have also carried out some measurements at the 5 extra locations marked with a star: $\mathbf{p_A} = (2.3, 3.5, 1)$m, $\mathbf{p_B} = (2.8, 3.48, 1)$m, $\mathbf{p_C} = (2.3, 4.0, 1)$m, $\mathbf{p_D} = (1, 5.9, 1)$m and $\mathbf{p_E} = (8.5, 5.85, 1)$m. Points $\mathbf{p_A}$, $\mathbf{p_B}$ and $\mathbf{p_C}$ were devised in order to test the FP algorithm in out-of-grid points, whereas points $\mathbf{p_D}$ and $\mathbf{p_E}$ were devised in order to test the algorithms in critical positions such as in the proximity of walls or corners. Finally, we highlight that the room was empty and free from in-band interference during the whole realization of the measurement campaign.
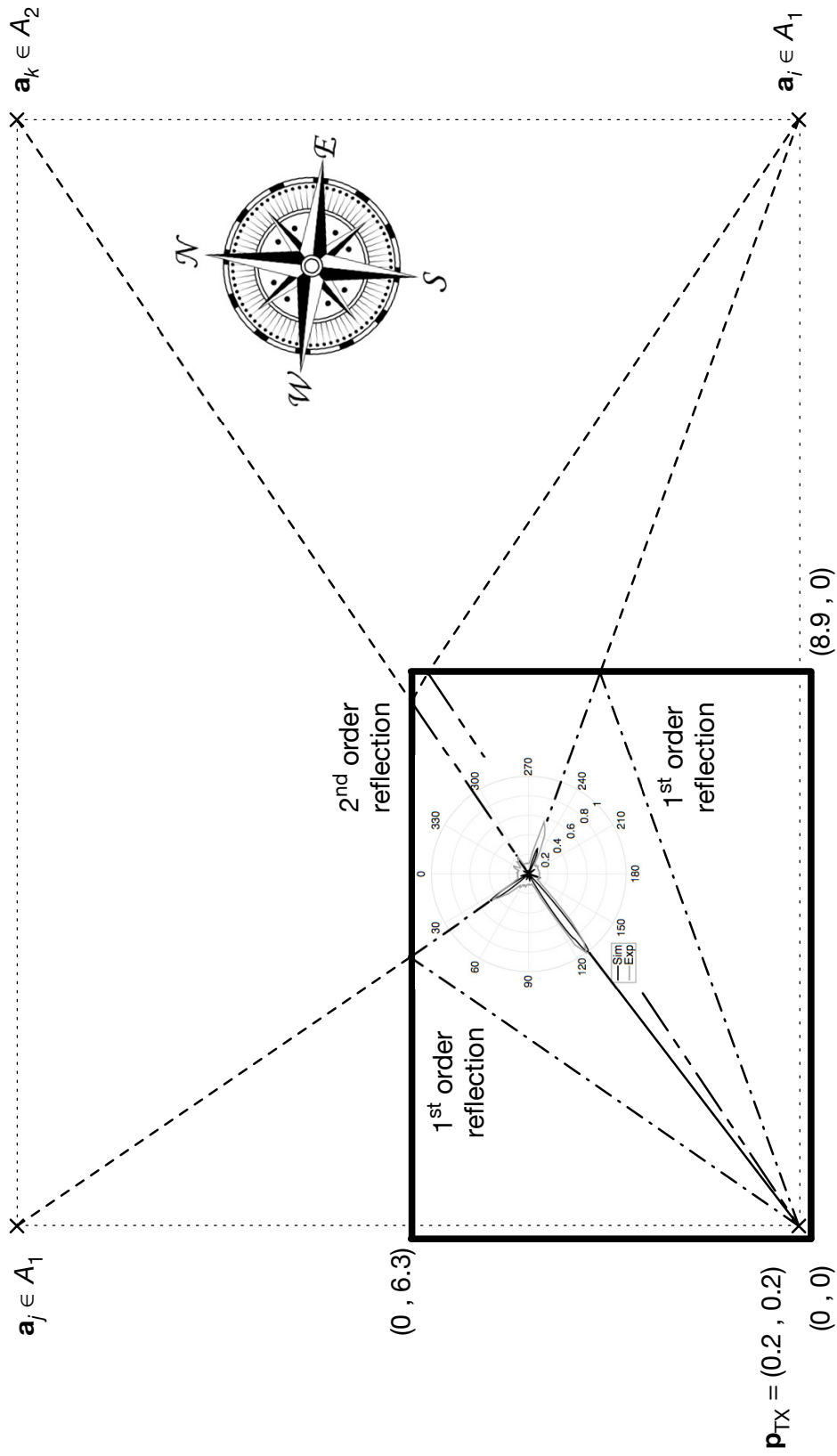
Figure 5.7: The AoA spectrum measured at position $(5.75, 4.45, 1)$m contextualized in the experiments' room. Notice the perfect agreement of the simulated and experimental AoAspectra with respect to the position of AP and the related VAs nodes resulting from the room geoemetry.

5.2 EXPERIMENTAL RESULTS

We tested the capability of the TV and ADoA algorithms to correctly localize a node located at each of the points in Figure 5.6. For the fingerprinting scheme, we used the measurements at the points in $\mathcal{F}_1$ as a training set, whereas those taken at the points in set $\mathcal{F}_2$ and at the points $\mathbf{p}_A$, $\mathbf{p}_B$, $\mathbf{p}_C$, $\mathbf{p}_D$ and $\mathbf{p}_E$ were employed to test the algorithm. As in Chapter 4, we characterized the performance of the algorithms in terms of the CDF of the localization error and of the probability P_u that a user cannot be localized. The TV and ADoA algorithms were configured to consider virtual anchors corresponding to up to either $\mu = 1$ or $\mu = 2$ reflections.

Figure 5.8 shows the CDF of the localization error for all schemes. The best performance is achieved by the ADoA algorithm with $\mu = 1$, for which $\approx 85\,\%$ of the measurements have sub-meter accuracy. However, as reported in Table 5.1, $P_u = 0.32$ in this case. By allowing ADoA to process second-order reflections ($\mu = 2$), only in four cases does the algorithm is unable to localize a node ($P_u = 0.09$). Being able to localize in more points, even those that are not localizable with $\mu = 1$, comes at the cost of larger estimation errors, as the CDF correspondingly shows sub-meter accuracy in $70\,\%$ of the cases.

The TV algorithm also shows lower errors in the $\mu = 1$ case with respect to the $\mu = 2$ case. This is because in the received power patterns, most of the time, the strongest peaks are relative to the LoS and the first order reflections. In any event, the probability of being able to localize a node is better for $\mu = 2$ ($P_u = 0.11$) than for $\mu = 1$ ($P_u = 0.16$). The fingerprinting algorithm shows a higher localization error, although it achieves $P_u = 0$. This is partly due to the choice of the measurement points in $\mathcal{F}_2$, which were taken at a maximal distance from the training set points in $\mathcal{F}_1$ in order to stress the FP algorithm. However, from the CDF we infer that about $55\,\%$ of the points are localized correctly at one of the nearest neighbors in the training set, whereas others tend to be localized farther due to the similarity of the measured AoA spectra. The poor performance of the FP algorithm is influenced by the normalization process involving the AoA spectra, as stated in Section 5.1.
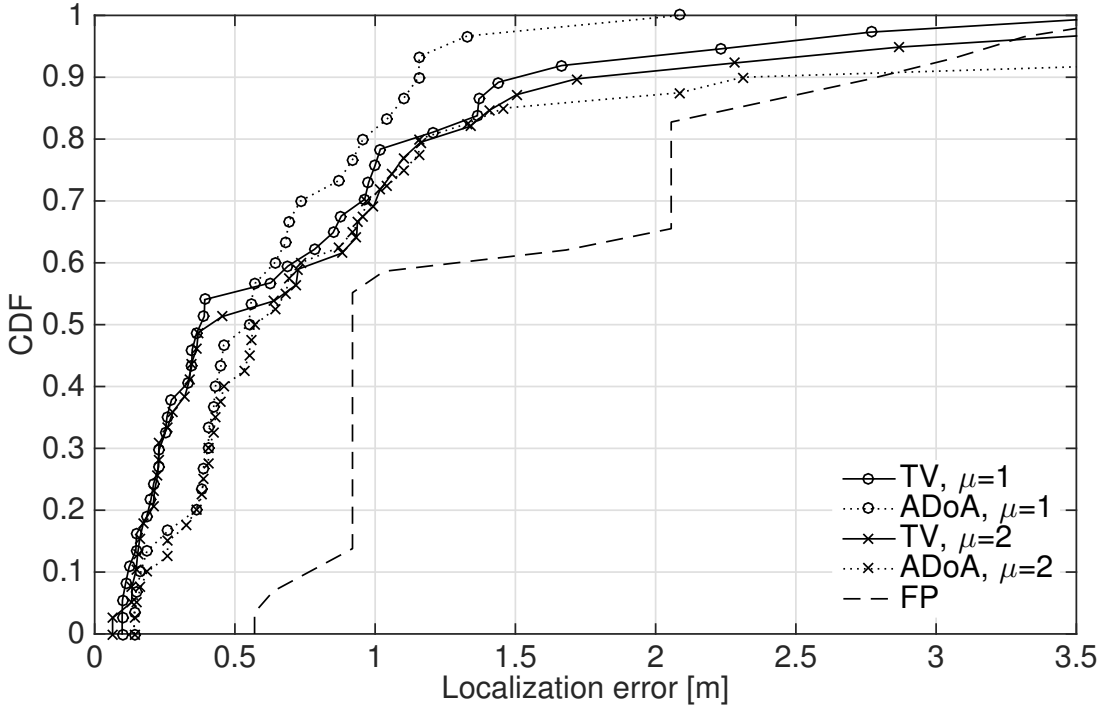
Figure 5.8: Experimental CDF of the localization error for all algorithms for different values of μ.

Table 5.1: P_u and probability of sub-meter accuracy for all algorithms.

	TV $\mu = 1$	TV $\mu = 2$	ADoA $\mu = 1$	ADoA $\mu = 2$	FP
P_u	0.16	0.11	0.32	0.09	0
$\mathbb{P}[\text{LE} \leq 1\,\text{m}]$	0.76	0.70	0.82	0.72	0.57

We conclude our analysis by showing the localization error of TV and ADoA ($\mu = 2$ in both cases) for each measurement point, and by marking which locations cannot be identified by each algorithm. These features are rendered in Figure 5.9 as a circle whose diameter is proportional to the error range. Those locations where the algorithms fail to estimate a position are indicated with a cross. Black markers refer to the TV algorithm, whereas gray markers refer to ADoA. Fingerprinting is not included in this graph due to the poor performance observed in Figure 5.8. We observe that the largest localization errors are primarily due to the large widths of some arrivals in the measured AoA spectra, which

make it difficult to accurately estimate the corresponding AoA. Specifically, for the locations near the transmitter, this is the case for the LoS AoA. Conversely, the weakness of the received signal and the presence of mainly second-order reflections in the AoA spectrum measured at the opposite corner of the room (point $\mathbf{p}_E$) explains why ADoA achieves a large error and TV is unable to localize. By comparing Figure 5.8 and Figure 4.2, we can also conclude that our measurements are affected by non-ideal conditions (related to the experimental equipment and setup) that induce an AoA estimation error with standard deviation on the order of $0.05 \,\mathrm{rad} = 2.86°$.

An interesting observation from Figure 5.9 is that none of TV and ADoA is successful at all locations, but they complement each other: where one fails, the other can compute an estimate, the accuracy of which depends on the location of the failure. In addition, the experimental results in Figure 5.8 suggest that it would be efficient to implement the algorithms so that they incrementally increase the cardinality of the anchor set $\mathcal{A}_\mu$ (and therefore their complexity) upon localization failures. In fact, for $\mu = 1$, we found that there is a fair chance to be able to localize a node, and the resulting estimate would help achieve a very good accuracy; the less accurate but more robust version of the two schemes ($\mu = 2$) may be invoked only in order to deal with localization failures.
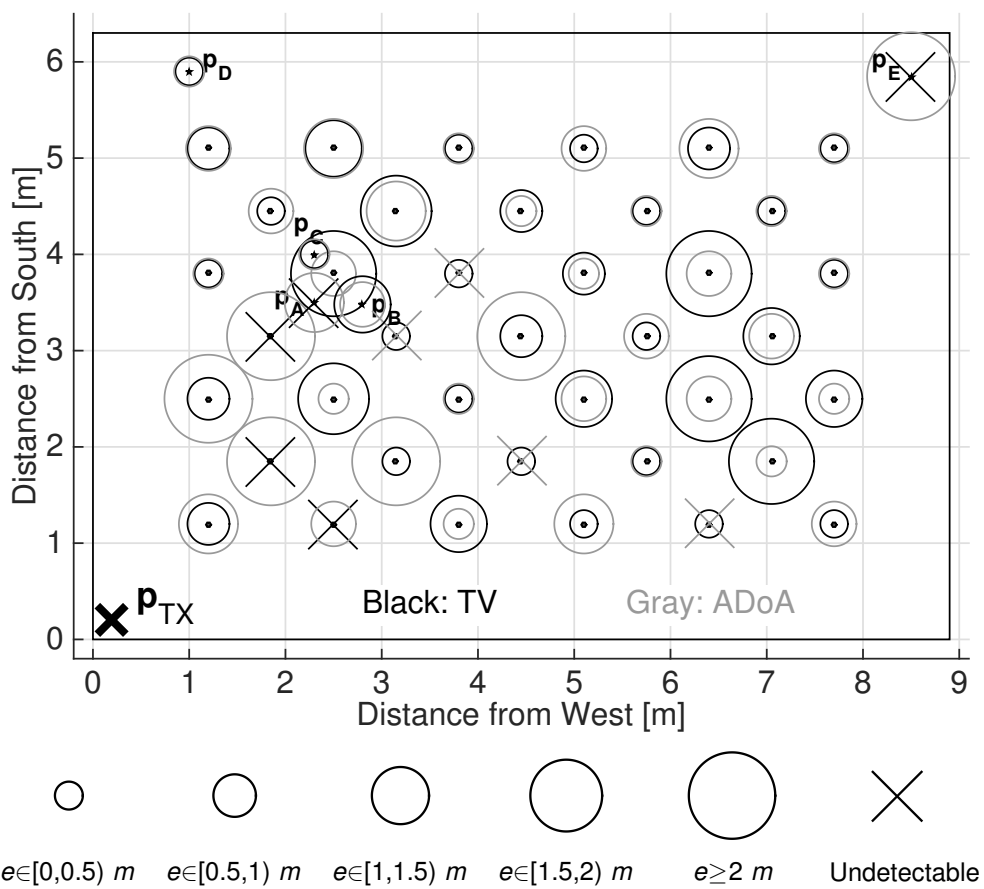
Figure 5.9: The measurements grid with the related errors in black for the TV algorithm and in gray for the ADoA algorithm.

6

CONCLUSIONS AND FUTURE WORK

In this thesis, we developed three different localization algorithms tailored around the characteristics of MilliMeter Wave (MMW) propagation, and able to localize a node subject to the presence of only a single Access Point (AP) by exploiting the AP signal reflections off the bounds of an environment with known geometry. One of the algorithms is based on a Triangulate-Validate (TV) procedure, a second one is based on Angle Difference-of-Arrival (ADoA), and a third one is based on location Fingerprinting (FP). All algorithms take as input what we have defined as Angle of Arrival (AoA) spectrum, that is a representation of the received power as a function of the azimuthal angle. A ray tracer tool has been developed in order to simulate AoA spectra in a user-defined environment. A performance evaluation has been carried out based on the simulated AoA spectra devising two quantities: the Localization Error (LE) which can be easily evaluated via its Cumulative Density Function (CDF), and the localization failure probability P_u. The ADoA algorithm resulted to be slightly more precise than the TV algorithm in the ideal case where the estimation of the AoA of the MultiPath Components (MPCs) is perfect; in this case, FP was outperformed by the other two algorithms: anyway, an improvement of the LE for the FP algorithm can be obtained increasing the training set cardinality. Introducing a zero mean and σ^2-variance normally-distributed error on the AoA estimation representing, e. g., incorrect beamforming, we concluded that, in general, the three algorithms are negatively affected. However, in this case FP resulted to be more resilient than TV and ADoA algorithms, and achieved a lower LE for values of $\sigma > 0.1$. We also evaluated the feasibility of the TV and ADoA algorithms when the AoA spectrum is sampled only once every $\Delta\phi$ [rad]: the algorithms performed similarly, both in terms of LE and localization failure probability. From the simulation we devised the value of $\Delta\phi^* = 3°$ as a good tradeoff to experimentally measure the AoA spectra exploiting a standard 60-GHz commercial hardware, such as the Dell

D5000 docking station and the Vubiq development system. Experimental results showed that, unless a large error affects AoA estimations, the algorithms achieve sub-meter accuracy with high probability, and feature a very low probability of localization failure. We finally observed that there is no absolute winner among the three algorithms, in that when one of them fails to localize, the others tend to succeed.

6.1 FUTURE WORK

The following is a list of possible future extensions that do not require the algorithms to be substantially modified. A natural continuation of the work would be to implement the algorithms in a mobile terminal. This translates to develop a unit able to continuously detect MPCs and finally extract a real time location estimate. Also, it would be interesting to implement the MUSIC or the ESPRIT algorithms to retrieve AoA information. Another interesting straightforward work would be to test the algorithms in the presence of double or multiple APs: this may be devised as a solution for localization in larger rooms, where a single AP would not be suitable to guarantee a sufficient number of MPCs. The addition of further APs is transparent to the TV and ADoA algorithms since it only translates into populating the partition subset A_0 with the positions of the multiple APs. This leads wider population of the set of virtual anchor nodes positions $\mathcal{A}_\mu$, for a given reflection order μ. A work aimed at strengthening the algorithms would be to take into account also Time of Arrival (ToA) and/or Time Difference of Arrival (TDoA) information. For example, for both TV and ADoA, time information may rule out some of the MPC$\leftrightarrow$Virtual Anchor (VA) associations, before having to try them. For the FP, the training may be extended to contain fingerprints based on AoA spectra as well as time information.

A future work where the TV and ADoA shall be revised is the following: presently, the algorithms permit to localize a node inside a room with known geometry, and a single AP with known location. The assumptions may be reversed: if we know the initial user position inside the room it should be possible

to determine the AP position and the room geometry. Initial guesses for the transmitter position may be done considering the strongest MPC that is likely coming from the transmitter. Then, based on the other MPCs, it should be possible to infer the position of the VAs. Finally, from the deployment of the transmitter and the related VAs, the room size and geometry may be devised.

In the remainder of this section we analyze related problems and discuss possible solutions about the actual scheme of the algorithms. First of all, the conditions in which we tested the algorithms were quasi-ideal: the experiments room was empty and free from signal interference. A further study would be necessary to test the algorithms' performance in the presence of furniture: a typical office environment presents a lot more obstacles than the walls, ceiling and floor we considered, thus unexpected MPCs may appear, and other expected MPCs may be shielded away from the receiver. This alters the localization process, possibly leading to localization errors. Certainly, when facing the presence of more obstacles that may cause unexpected reflections, a solution would be to populate the set $\mathcal{Z}$ with those objects, but this would lead to an exponential growth of the virtual anchor subsets' cardinality, impacting the complexity of the algorithms. Thus, a preliminary study may be carried out by simulating the algorithms performances over AoA spectra where MPCs are removed or randomly added. Based on the obtained results, it would be possible to devise a characterization of the obstacles that really need to be taken into account and added to $\mathcal{Z}$.

Apart from the furnished case, unexpected MPCs may appear if the receiver is equipped with a non-perfectly directional antenna, i.e., with sidelobes. To better understand the problem we devise the following example: let the receiver antenna has a reception beam pattern with a main lobe and two smaller sidelobes; if no MPCs reach the antenna in the main lobe direction, there may be a power contribution as well if some MPC reaches the other two sidelobes; this means that, for a given direction, we are sensing a MPC that, in reality, does not exits, and clearly, this may lead to localization errors. A possible solution to this would be to estimate the reception beam pattern of the antenna and perform a sort of decorrelation with the measured AoA spectrum.

Another non-ideal case may be the presence of time-varying MPCs. This may be the consequence of people or objects moving inside the environment. The problem could be mitigated by exploiting the temporal correlation between AoA spectra. Another study related to temporal correlation would be movement estimation: the variation of the MPCs may be exploited in order to track a user inside the room and also strengthen the localization estimate thanks to the correlation. To this purposehre, the employment of a Kalman Filter (KF) shall be considered.

BIBLIOGRAPHY

[1] International Telecommunication Union (ITU), "Radio Regulations." [Online]. Available: http://www.itu.int/dms_pub/itu-s/oth/02/02/S02020000244501PDFE.PDF

[2] T. Rappaport *et al.*, *Millimeter Wave Wireless Communications.* Pearson Education, 2014.

[3] S. Rangan, T. Rappaport, and E. Erkip, "Millimeter-wave cellular wireless networks: Potentials and challenges," *Proceedings of the IEEE*, vol. 102, no. 3, pp. 366–385, Mar. 2014.

[4] J. Thompson *et al.*, "5G wireless communication systems: prospects and challenges," *IEEE Commun. Mag.*, vol. 52, no. 2, pp. 62–64, Feb. 2014.

[5] T. Rappaport *et al.*, "Millimeter wave mobile communications for 5G cellular: It will work!" *IEEE Access*, vol. 1, pp. 335–349, 2013.

[6] I. S. Association, "802.11ad-2012." [Online]. Available: https://standards.ieee.org/findstds/standard/802.11ad-2012.html

[7] B. Cook *et al.*, "Indoor location using trilateration characteristics," in *Proc. London Communications Symposium*, London, UK, Sep. 2005.

[8] G. R. MacCartney *et al.*, "Path loss models for 5G millimeter wave propagation channels in urban microcells," in *Proc. IEEE GLOBECOM*, Atlanta, GA, Dec. 2013.

[9] F. Giannetti, M. Luise, and R. Reggiannini, "Mobile and personal communications in the 60 GHz band: A survey," *Springer Wireless Personal Communications*, vol. 10, no. 2, pp. 207–243, 1999.

[10] E. Torkildson, H. Zhang, and U. Madhow, "Channel modeling for millimeter wave MIMO," in *Proc. Information Theory and Applications Workshop*, San Diego, CA, Jan. 2010.

[11] A. Maltsev *et al.*, "Experimental investigations of 60 GHz WLAN systems in office environment," *IEEE J. Sel. Areas Commun.*, vol. 27, no. 8, pp. 1488–1499, Oct. 2009.

[12] National Coordination Office for Space-Based Positioning, Navigation, and Timing, "Space Segment." [Online]. Available: http://www.gps.gov/systems/gps/space/

[13] N. Ashby, "Relativity in the global positioning system," *Living Reviews in Relativity*, vol. 6, no. 1, Jan. 2003.

[14] Y. O. *et al.*, "Field strength variability in VHF and UHF land mobile service," *fsdakjlfkljadshflksa*, vol. 16, pp. 825–873, Oct. 1968.

[15] T. Kos, M. Grgic, and G. Sisul, "Mobile user positioning in gsm/umts cellular networks," in *Multimedia Signal Processing and Communications, 48th International Symposium ELMAR-2006 focused on*, Zadar, Croatia, Jun. 2006.

[16] Hui Liu *et al.*, "Survey of wireless indoor positioning techniques and systems," *IEEE Trans. Syst., Man, Cybern. C*, vol. 37, no. 6, pp. 1067–1080, Nov. 2007.

[17] L. Redlin and N. V. S. Watson, "Thales' shadow," *Mathematics Magazine*, vol. 73, no. 5, pp. 347–353, Dec. 2000.

[18] R. Schmidt, "Multiple emitter location and signal parameter estimation," *IEEE Trans. Antennas Propag.*, vol. 34, no. 3, pp. 276–280, Mar. 1986.

[19] R. Roy and T. Kailath, "Esprit-estimation of signal parameters via rotational invariance techniques," *IEEE Trans. Acoust., Speech, Signal Process.*, vol. 37, no. 7, pp. 984–995, Jul. 1989.

[20] K. Kaemarungsi and P. Krishnamurthy, "Modeling of indoor positioning systems based on location fingerprinting," in *Proc. IEEE INFOCOM*, Hong Kong, China, Mar. 2004.

[21] C. Laoudias, D. Zeinalipour-Yazti, and C. G. Panayiotou, "Crowdsourced indoor localization for diverse devices through radiomap fusion," in *Proc. IPIN*, Montbeliard-Belfort, France, Oct. 2013.

[22] J. Xiong and K. Jamieson, "Arraytrack: A fine-grained indoor location system," in *Proc. USENIX*, Lombard, IL, Apr. 2013.

[23] Sen Souvik *et al.*, "Avoiding multipath to revive inbuilding WiFi localization," in *Proc. MobiSys*, Taipei, Taiwan, Jun. 2013.

[24] R. Nandakumar, K. K. Chintalapudi, and V. Padmanabhan, "Centaur: Locating devices in an office environment," in *Mobicom*, Istanbul, Turkey, Aug. 2012.

[25] Alex Mariakakis *et al.*, "SAIL: Single access point-based indoor localization," in *Proc. MobiSys*, Bretton Woods, NH, Jun. 2014.

[26] L. Banin, U. Schtzberg, and Y. Amizur, "Next generation indoor positioning system based on wifi time of flight," in *Proc. ION GNSS+*, Nashville, TN, Sep. 2013.

[27] J. Kunisch and J. Pamp, "An ultra-wideband space-variant multipath indoor radio channel model," in *Proc. IEEE UWST*, Reston, VA, Nov. 2003.

[28] P. Meissner, C. Steiner, and K. Witrisal, "UWB positioning with virtual anchors and floor plan information," in *Proc. WPNC*, Dresden, Germany, Mar. 2010.

[29] P. Meissner, T. Gigl, and K. Witrisal, "UWB sequential monte carlo positioning using virtual anchors," in *Proc. IPIN*, Zurich, Switzerland, Sep. 2010.

[30] P. Meissner and K. Witrisal, "Multipath-assisted single-anchor indoor localization in an office environment," in *Proc. IWSSIP*, Vienna, Austria, Apr. 2012.

[31] P. Meissner *et al.*, "Analysis of an indoor UWB channel for multipath-aided localization," in *Proc. IEEE ICUWB*, Bologna, Italy, Sep. 2011.

[32] ——, "Accurate and robust indoor localization systems using ultra-wideband signals," in *Proc. ENC*, Vienna, Austria, Apr. 2012.

[33] C. Gentner and T. Jost, "Indoor positioning using time difference of arrival between multipath components," in *Proc. IPIN*, Montbeliard-Belfort, France, Oct. 2013.

[34] K. Witrisal and P. Meissner, "Performance bounds for multipath-assisted indoor navigation and tracking (MINT)," in *Proc. IEEE ICC*, Ottawa, Canada, Jun. 2012.

[35] D. Emerson, "Jagadis chandra bose: millimetre wave research in the nineteenth century," in *Proc. TENCON '98*, New Delhi, India, Dec. 1998.

[36] A. Osseiran *et al.*, "Scenarios for 5G mobile and wireless communications: the vision of the METIS project," *IEEE Commun. Mag.*, vol. 52, no. 5, pp. 26–35, May 2014.

[37] A. Sayeed, "Deconstructing multiantenna fading channels," *IEEE Trans. Signal Process.*, vol. 50, no. 10, pp. 2563–2579, Oct. 2002.

[38] D. Mavrakis and S. R. Saunders, "A delay-centred wideband indoor channel model for MM-wave communications," in *Proc. ICAP*, Exeter, UK, Mar. 2003.

[39] A. Y. Nashashibi, "Microwave and millimeter-wave propagation and scattering in dense random media: modeling and experiments," Ph.D. dissertation, University of Michigan, Ann Arbor, MI, Sep. 1995.

[40] E. S. Li and K. Sarabandi, "Low grazing incidence millimeter-wave scattering models and measurements for various road surfaces," *IEEE Trans. Antennas Propag.*, vol. 47, no. 5, pp. 851–861, May 1999.

[41] A. Salcedo, "Radiative transfer theory for scattering by large cylindrical disk scatterers," Master's thesis, Massachusetts Institute of Technology, Cambridge, MA, May 1994.

[42] A. Sentenac, H. Giovannini, and M. Saillard, "Scattering from rough inhomogeneous media: splitting of surface and volume scattering," *JOSA A*, vol. 19, no. 4, pp. 727–736, apr 2002.

[43] L. Subrt, P. Pechac, and S. Zvanovec, "New approach to modeling of diffuse reflection and scattering for millimeter-wave systems in indoor scenarios," *PIERS Online*, vol. 6, 2010.

[44] H. Xu, V. Kukshya, and T. Rappaport, "Spatial and temporal characteristics of 60-GHz indoor channels," *IEEE J. Sel. Areas Commun.*, vol. 20, no. 3, pp. 620–630, Apr. 2002.

[45] C. R. Lomba, R. T. Valadas, and A. M. de O. Duarte, "Experimental characterization and modeling of the reflection of infrared signals on indoor sur-

faces," *IEE Proceedings - Optoelectronics*, vol. 145, no. 3, pp. 191–197, Jun. 1998.

[46] N. Peinecke, H. Doehler, and B. Korn, "Phong-like lighting for MMW radar simulation," in *Proc. SPIE*, Cardiff, UK, 2008.

[47] H. El-Sayed, G. Athanasiou, and C. Fischione, "Evaluation of localization methods in millimeter-wave wireless systems," in *Proc. IEEE CAMAD*, Athens, Greece, Dec. 2014.

[48] A. Jafari *et al.*, "NLOS influence on 60 GHz indoor localization based on a new TDOA extraction approach," in *Proc. EuMC*, Nuremberg, Germany, Oct. 2013.

[49] F. W. *et al.*, "A 60 ghz ofdm indoor localization system based on dtdoa," in *14th IST Mobile and Wireless Communication Summit*, Dresden, Germany, Jun. 2005.

[50] H. Deng and A. Sayeed, "Mm-wave MIMO channel modeling and user localization using sparse beamspace signatures," in *Proc. IEEE SPAWC*, Toronto, Canada, Jun. 2014.

[51] T. H. Cormen *et al.*, *Introduction to Algorithms.* MIT Press and McGraw-Hill, 2001.

[52] N. Moraitis and P. Constantinou, "Indoor channel measurements and characterization at 60 GHz for wireless local area network applications," *IEEE Trans. Antennas Propag.*, vol. 52, no. 12, pp. 3180–3189, 2004.

[53] R. E. *et al.*, "Overview of spatial channel models for antenna array communication systems," *IEEE Personal Commun. Mag.*, vol. 5, no. 1, pp. 10–22, Feb. 1998.

ACRONYMS

μW   microwave

ADoA   Angle Difference-of-Arrival

AoA   Angle of Arrival

AP   Access Point

CDF   Cumulative Density Function

CIR   Channel Impulse Response

EHF   Extremely High Frequency

EKF   Extended Kalman Filter

FP   Fingerprinting

GPS   Global Positioning System

IoT   Internet of Things

IPS   Indoor Positioning System

ITU   International Telecommunication Union

KF   Kalman Filter

LE   Localization Error

LoS   Line of Sight

MIMO   Multiple-Input Multiple-Output

ML   Maximum Likelihood

MMW   MilliMeter Wave

MPC   MultiPath Component

MUSIC   MUltiple SIgnal Classification

NLoS   Non-Line of Sight

OFDM   Orthogonal Frequency Division Multiplexing

OTDoA   Observed Time Difference of Arrival

PAP   Power Amplitude Profile

PDP   Power Delay Profile

PF   Particle Filter

PHY   PHYsical layer

RF   Radio Frequency

RSS   Received Signal Strength

SHF   Super High Frequency

TDoA   Time Difference of Arrival

ToA   Time of Arrival

TV   Triangulate-Validate

UE   User Equipment

UWB   Ultra Wide Band

VA   Virtual Anchor

WiFi   Wireless Fidelity

WLAN   Wireless Local Area Network

Twenty years from now you will be more disappointed
by the things that you didn't do than by the ones you did so.
So throw off the bowlines. Sail away from the safe harbor.
Catch the trade winds in your sails. Explore. Dream. Discover.

— Mark Twain

ACKNOWLEDGMENTS

This thesis is the result of my abroad experience in Madrid and would not have been possible without knowing Paolo Casari. It all began choosing 8 from a numbered list of projects Professor Michele Zorzi assigned us for a course project in Network Analysis an Simulations. Paolo, from the very first moment we met, has shown himself to be a very kind and lowly person, a person from which you can learn a lot. The project kept going on, we get enough results to be presented as the final course project, but still there were things that required to be investigated further. Time goes by, the second semester was approaching, a proposal from Paolo that in the meanwhile moved to the IMDEA Networks Institute in Madrid: why don't you come here at IMDEA for your Master's Thesis? Such occasions do not have to be missed and I left. We concluded the work left, that resulted in my first publication, and started working for this thesis that now comes to the end. I will be forever grateful to Paolo for this opportunity he gave me, for his patience, for the lot of things I learned from him, for being a good friend, not only a professor.

A proper thanks goes to Professor Michele Zorzi, for his teachings, for the supervisioning during my stay abroad, and for the lot of time he dedicated to me. I can do no other than express my utmost appreciation to him.

A particular person I would like to thank is Bruno Tollot, the secondary-school professor which passionated my about Electronics and Telecommunications. Still I am grateful to him and I will always be grateful for his teachings, for the opportunities he gave me, for having been such a professor that would need to be taken as an example for everyone.